AIAA JOURNAL
Vol. 61, No. 3, March 2023

Evaluating Dynamic Stall-Onset Criteria for Mixed and Trailing-Edge Stall

Sarasija Sudharsan*
Iowa State University, Ames, Iowa 50011
Shreyas Narsipur†
Mississippi State University, Mississippi State, Mississippi 39762
and
Anupam Sharma‡
Iowa State University, Ames, Iowa 50011

https://doi.org/10.2514/1.J062011

We evaluate two leading-edge-based dynamic stall-onset criteria (namely, the maximum magnitudes of the leading-edge suction parameter and the boundary enstrophy flux) for mixed and trailing-edge stall. These criteria have been shown to successfully predict the onset of leading-edge stall at Reynolds numbers of $\sim\mathcal{O}(10^5)$, where the leading-edge suction drops abruptly. However, for mixed/trailing-edge stall, leading-edge suction tends to persist even when there is significant trailing-edge reversed flow and stall is underway, necessitating further investigation into the effectiveness of these criteria. Using wall-resolved large-eddy simulations and the unsteady Reynolds-averaged Navier–Stokes method, we simulate one leading-edge stall and three mixed/trailing-edge stall cases at Reynolds numbers of 2×10^5 and 3×10^6. We contrast the progression of flow features such as trailing-edge separation and vortex formation across different stall types and evaluate the stall-onset criteria relative to critical points in the flow. We find that the criteria nearly coincide with the instance of leading-edge suction collapse and are reached in advance of dynamic stall vortex formation and lift stall for all four cases. We conclude that the two criteria effectively signal dynamic stall onset in cases where the dynamic stall vortex plays a prominent role.

I. Introduction

DYNAMIC stall is a topic of great interest in unsteady aerodynamics due to its severity compared to static stall [1]. It occurs over aerodynamic surfaces undergoing large-amplitude transient motion or unsteady maneuvers, for example, over wind turbine or helicopter rotor blades. The large unsteady aerodynamic loads that are incurred due to dynamic stall can lead to structural damage or failure. This has led to several studies on flow control using leading-edge blowing [2,3], plasma actuation [4,5], synthetic jets [6], etc. However, the timely application of these control efforts is important because they are most effective before the formation of the dynamic stall vortex (DSV) [7], which is a coherent vortex structure that is a characteristic feature of "deep" stalls [1]. Characterizing stall onset is of crucial importance for these control efforts to be deployed in a timely manner.

Various criteria for dynamic stall onset based on the unsteady aerodynamic coefficients have been explored to formulate first-order semiempirical, dynamic stall models [8,9]. However, our interest is in narrowing down the identification of the stall onset point to a finer degree. Currently, the leading-edge suction parameter (LESP), which a measure of the chordwise suction force near the leading edge [10], is widely used for identifying dynamic stall onset [11–14]. It was used in a low-order model to trigger leading-edge vortex shedding when a predetermined [from computational fluid dynamics (CFD)] critical value was reached. Recent work using the statistics of pressure distributions over the airfoil surface [15,16] has indicated critical points in the motion, including laminar separation bubble (LSB) initiation, DSV initiation, and DSV detachment. Narsipur et al. [17] presented an approach to calculate the LESP from CFD as a scaled force in the camber direction, with a dynamic pressure scaling based on the relative velocity of the airfoil. While several of the aforementioned works have used a pressure-based approach to identifying stall onset, Sudharsan et al. [18] proposed a vorticity-based criterion. They demonstrated that the boundary enstrophy flux (BEF) signals leading-edge stall onset by reaching its maximum magnitude earlier than the LESP, based on wall-resolved large-eddy simulations (LES) at chord-based Reynolds numbers Re_c of 2×10^5 and 5×10^5.

In the present work, we consider the max(LESP) and max(|BEF|) criteria to study the effectiveness of leading-edge-based parameters in signaling mixed and trailing-edge stall. We anticipate that the DSV initiation point obtained from C_p statistics is likely to lie close to the maxima of |BEF| and LESP because it captures the leading-edge suction collapse; therefore, we do not consider it here. Detailed descriptions of different stall types have been well documented in the literature [19–21]. The use of the LESP for different Re_c and kinematics has been explored as well [10,17]. However, the comparison of stall criteria applied specifically to each type of stall is a novel contribution from the present work. Sudharsan et al. previously compared the BEF parameter to the LESP for leading-edge stall [18]. The results of preliminary investigations into the effectiveness of the max(LESP) and max(|BEF|) criteria in signaling mixed and trailing-edge stall have been presented in a conference paper [22]. The current work presents those results and builds on them to examine the effectiveness of the two criteria in indicating dynamic stall in DSV-dominated flows with significant trailing-edge separation. The conclusions from this study can enable the judicious use of LESP and BEF in dynamic stall models.

II. Problem Description

We begin by describing the flow characteristics of different stall types to illustrate why significant trailing-edge separation poses a challenge for leading-edge-based stall criteria.

Presented as Paper 2022-1983 at the AIAA Scitech 2022 Forum, San Diego, CA and Virtual, January 3–7, 2022; received 8 June 2022; revision received 13 October 2022; accepted for publication 19 November 2022; published online 29 December 2022.

*Graduate Student, Department of Aerospace Engineering.
†Assistant Professor, Department of Aerospace Engineering. Senior Member AIAA.
‡Associate Professor, Department of Aerospace Engineering. Associate Fellow AIAA.

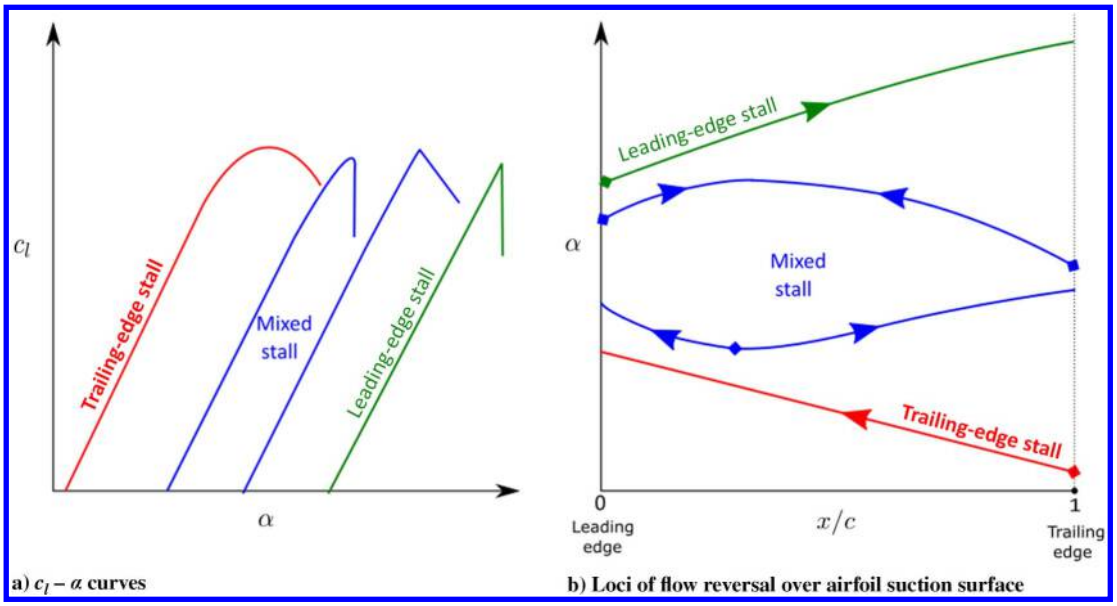

Fig. 1 Schematics showing conventional understanding of leading-edge, mixed, and trailing-edge stall. Figure 1a was adapted from Ref. [19].

Figure 1a represents the conventional understanding [19,23] of leading-edge stall as being relatively abrupt in the variation of aerodynamic coefficients, with trailing-edge stall being more gradual and mixed stall having characteristics of both. The peak in C_l is rounded for the trailing-edge stall case, and the subsequent dropoff occurs gradually. In contrast, C_l drops abruptly for leading-edge stall due to the formation of a stronger and more compact DSV [20,24] moving away from the airfoil surface. Finally, a mixed stall case could have either a rounded peak with an abrupt dropoff or a sharp peak with a gradual drop in C_l, as shown in the figure. The former might occur when trailing-edge reverse flow moves slowly upstream, leading to the rounding of the lift curve, but culminates in an abrupt stall due to leading-edge flow breakdown. The latter could occur when trailing-edge reverse flow moves upstream abruptly, leading to a relatively sharp peak [23], although the subsequent drop in lift is less abrupt as compared to leading-edge stall. These variations are also reflected in the other unsteady aerodynamic coefficients, such as the coefficients of the drag C_d and moment C_m. In general, DSV formation is expected closer to the leading edge for leading-edge stall and further aft for trailing-edge stall.

Figure 1b shows the loci of the most upstream points of boundary-layer flow reversal over the airfoil suction surface with increasing α for different stall types, as previously identified by McCroskey et al. [21]. In a classic leading-edge stall [21], the collapse in leading-edge suction (instance of $\max(|C_p|)$ near the leading edge) is accompanied by the bursting of the LSB and leads to the formation of a DSV close to the leading edge with little or no trailing-edge separation. Flow reversal propagates downstream from the leading edge, as shown by the green curve in Fig. 1b. However, a trailing-edge stall [25] occurs due to instabilities arising in the reversed flow moving upstream from the trailing edge (red curve in Fig. 1b). Leading-edge suction persists even after a large region of reverse flow has formed downstream [23]. DSV formation occurs when the trailing-edge reverse flow reaches the leading edge. This is a significantly different sequence of events as compared to leading-edge stall. Therefore, in a purely trailing-edge stall, there is no distinct *leading-edge* boundary-layer separation [21]. From their recent experimental work, Kiefer et al. [26] observed gradual trailing-edge dynamic stall, with continually attached leading-edge flow, for a NACA 0021 airfoil at Re_c ranges of 0.5×10^5–5×10^6. This poses a challenge for stall-onset criteria focused on the leading-edge region because stall onset might not be indicated until the trailing-edge reverse flow reaches the leading edge: by which time, *lift stall* might have occurred. Boundary-layer separation can also exhibit characteristics of both leading- and trailing-edge stall. In such a "mixed" stall scenario, two distinct boundary-layer disturbances occur, both near the leading edge and the trailing edge, with their subsequent merging/interaction [21]. This would be reflected in the C_f distribution with negative values over the entire airfoil suction surface during the time of their interaction. Benton and Visbal [27] found for a pitching NACA 0012 airfoil at $Re_c = 10^6$ that LSB bursting is initiated when turbulent separation from the trailing edge reaches the bubble. Similar observations were made by Sharma and Visbal [28] for the much thicker NACA 0018 airfoil at $Re_c = 2 \times 10^5$. Alternately, a disturbance first occurring near midchord could propagate both upstream and downstream. The blue curves in Fig. 1b represent these two variations of mixed stall. In the present work, we classify the type of stall using the locus of initial boundary-layer flow reversal as a guide.

Our objective is to evaluate the two stall-onset criteria, max(LESP) and max(|BEF|), for mixed and trailing-edge stall. We have used the maximum LESP as a proxy for the critical LESP value because max(LESP) is a standalone criterion that can be evaluated without a priori knowledge of the critical LESP value. Note that this assumption is valid for the Re_c under consideration but will not hold for $Re_c \leq \mathcal{O}(10^4)$, based on results from Narsipur et al. [17]. Additionally, the present study is limited to incompressible flows. We evaluate the aforementioned criteria relative to the instance of critical points such as DSV formation and lift stall. We also describe the progression of flow events for different stall types based on the four cases considered. As the dynamics of the vortex are harder to control once it has rolled up, a key point of interest is to ascertain if the two parameters reach their maximum values before DSV rollup occurs so that effective control measures can be deployed. We consider only those cases where the DSV plays a dominant role in the stall process in the presence of significant trailing-edge separation. We identify DSV formation from streamlines, as well as C_p and C_f distributions over the airfoil surface (appendix B of Sudharsan et al. [18] provided a detailed description of DSV identification). The effectiveness of the stall-onset criteria is evaluated by comparing the times when the criteria are reached relative to the instant of DSV formation.

The following section (Sec. III) details the CFD methods used, the cases considered, and the LESP and BEF parameters. Section IV presents and analyzes the results from the current investigations, and Sec. V summarizes the conclusions drawn.

III. Methods and Details

A. Computational Methodology

Our results are based on two types of numerical simulations: wall-resolved LES and unsteady Reynolds-averaged Navier–Stokes (URANS). LES was carried out using the compressible flow solver, FDL3DI [28,29], where the effect of subgrid-scale (SGS) stresses is

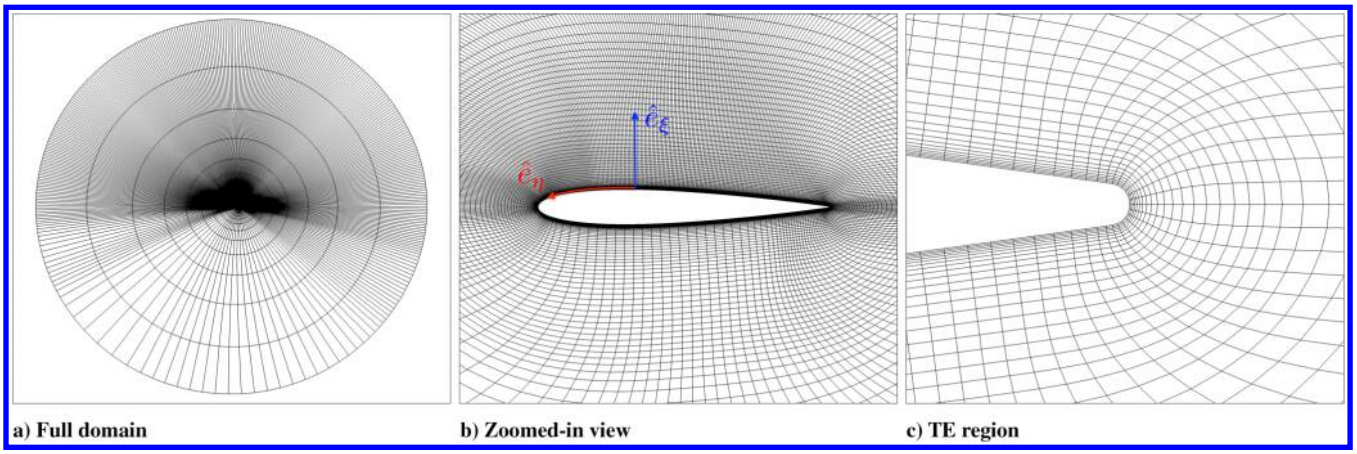

Fig. 2 Mesh used for LES with every fifth and every fourth points in the radial and circumferential directions shown: a) full domain; b) zoomed-in view near airfoil, identifying radial $\hat{e}_\xi$ and circumferential $\hat{e}_\eta$ directions; and c) zoomed-in view showing trailing-edge geometry.

modeled implicitly by spatial filtering at each time step to remove energy at unresolved scales. Spatial discretization uses a sixth-order compact difference scheme, whereas time integration is carried out using an implicit, approximate factorization technique. The implicit LES approach has been shown (see, e.g., Refs. [30,31]) to give results of quality equal to the traditional LES approach of explicitly modeling SGS stresses.

The spatial domain is discretized using a single-block O mesh around the airfoil, which is repeated with uniform mesh spacing along the span. The O grid in the physical space (x, y, z) maps to an H grid in the computational domain (ξ, η, ζ). Figure 2 shows the overall computational domain and zoomed-in views of the mesh around the airfoil and in the trailing-edge region. The following orientation is used: $\hat{e}_\xi$ points radially out, $\hat{e}_\eta$ is in the circumferential direction, and $\hat{e}_\zeta$ (obtained following the right-hand rule) is in the span direction.

Freestream conditions are prescribed at the outer boundary, which is about 99 chords away from the airfoil. The filtering procedure removes all perturbations as the mesh becomes coarse away from the airfoil to the far-field boundary. Periodic boundary conditions are imposed at the span boundaries. The span of the airfoil model is equal to 10% of the airfoil chord, which has been shown to be sufficient for dynamic stall simulations by Sharma and Visbal [28].

Based on the grid sensitivity study presented in Appendix A.1, we used a grid having 410, 1341, and 134 grid points in the radial, circumferential, and spanwise directions, respectively. The chosen mesh is highly refined over the suction surface to capture small-scale viscous flow features. A statistically stationary solution was first obtained for a static simulation with the angle of attack α fixed at 4 deg. C_p and C_f distributions over the airfoil were compared with XFOIL (a program to design and analyze subsonic isolated airfoils) and found to be in good agreement. Next, the dynamic pitching motion was simulated through grid motion, with a ramp function that smoothly transitions to the required pitch rate. The results presented are based on two-dimensional (2-D) flowfields obtained by span-averaging the three-dimensional solution. Details on the solver, grid, and verification of results were discussed extensively by Sharma and Visbal [28].

The URANS simulations were performed using the REACTMB-INS code, which solves the time-dependent incompressible Navier–Stokes equations using a finite volume method. The governing equations are written in the arbitrary Lagrangian/Eulerian form, which enables the motion of a body-fitted computational mesh in accord with prescribed rate laws. Spatial discretization of the inviscid fluxes uses a low-diffusion flux-splitting method valid in the incompressible limit [32]. This method is extended to higher-order spatial accuracy using piecewise parabolic method interpolations of the primitive variables $[p, u, v, w]^T$ and the transported variable for the Spalart–Allmaras model $\tilde{\nu}$. Viscous terms are discretized using second-order central differences. A dual time-stepping method is used to integrate the equations in time. An artificial compressibility technique, discretized in a fully implicit fashion and solved approximately using Incomplete Lower and Upper (ILU) factorization, is used to advance the solution in pseudotime. Typically, eight subiterations per physical time step were needed to reduce the residuals by two orders of magnitude. The Spalart–Allmaras model [33] as implemented by Edwards and Chandra [34] is used for turbulence closure. A two-dimensional body-fitted O grid containing 140,400 cells was generated for the URANS simulations. A grid sensitivity study, carried out to ensure grid convergence, showed that decreasing the wall y^+ to one-tenth of that used in the final grids does not alter the results noticeably; a summary of the grid sensitivity study is presented in Appendix A.2. The current URANS methodology has been validated against data from wind- and water-tunnel experiments for various unsteady airfoil motions in Refs. [10,11,35].

B. Datasets Used

Details on the cases discussed in the current paper (airfoil geometries, Re_c, kinematics, etc.) are listed in Table 1. We simulated airfoils pivoted about the quarter-chord point undergoing either a constant-rate pitch-up (LE and MX cases) or a pitch-up–return motion generated using Eldredge et al.'s [24] canonical formulation [mixed/trailing-edge (MXTE) and TE cases; see the work of Narsipur et al. [17] for details]. The ramp cases (LE and MX) were carried out using a LES at a moderate Re_c of 2×10^5, whereas the pitch-up–return cases (MXTE and TE) were simulated using URANS at a higher Re_c of 3×10^6.

Table 1 Datasets used in present work[a]

Case	Airfoil	Re_c	Simulation type	Kinematics	Stall type
LE	NACA 0012	2×10^5	LES and URANS	Constant pitch-up, $\alpha_{max} = 26$ deg, $K = 0.025$	Leading edge
MX	NACA 0018	2×10^5	LES	Constant pitch-up, $\alpha_{max} = 30$ deg, $K = 0.025$	Mixed
MXTE	NACA 0012	3×10^6	URANS	Pitch-up–return, $\alpha_{max} = 45$ deg, $K = 0.075$	Mixed/trailing edge
TE	NACA 0012	3×10^6	URANS	Pitch-up–return, $\alpha_{max} = 45$ deg, $K = 0.025$	Trailing edge

[a]The pivot location of the pitching motion is at $x = 0.25c$ for all cases, and $Ma = 0.1$ for all LES cases.

A ramp function $\Omega^+(t)$ defined by Eq. (1) was used for the LES cases to smoothly transition the pitch rate from zero at $t^* = 0$ to its final value of 0.025 at $t^* = t_0$ (details are in Ref. [28]). For $t^* > t_0$, the airfoil continues to pitch up at a constant rate of 0.025. Note that s is a scaling parameter that determines the steepness of the ramp function. Also, $s = 2.0$ and $t_0 = 0.35$ were used for the simulations:

$$\Omega^+(t) = K\left(\frac{\tanh(s(2(t/t_0)-1)) + \tanh(s)}{1+\tanh(s)}\right) \tag{1}$$

The pitch-up–return motions, generated for the URANS cases, were defined using a smoothing function $G(t)$ as a function of time t as [24]

$$G(t) = \ell_n\left[\frac{\cosh(aU_\infty(t-t_1)/c)\cosh(aU_\infty(t-t_4)/c)}{\cosh(aU_\infty(t-t_2)/c)\cosh(aU_\infty(t-t_3)/c)}\right] \tag{2}$$

where a is a smoothing parameter from Ref. [36] given by

$$a = \frac{\pi^2 K}{2\alpha_{\text{amp}}(1-\sigma)} \tag{3}$$

where α_{amp} is the amplitude of the pitching motion, and K is the nondimensional pitch rate ($K = \dot{\alpha}c/2U_\infty$). The symbols t_1 to t_4 are defined as follows: t_1 is the time from reference 0 until the start of the ramp, $t_2 = t_1 + \alpha_{\text{amp}}/2K$, $t_3 = t_2 + \pi\alpha_{\text{amp}}/4K - \alpha_{\text{amp}}/2K$, and $t_4 = t_3 + \alpha_{\text{amp}}/2K$. The variation of pitch during the motion is then given by

$$\alpha(t) = \alpha_{\text{amp}}\frac{G(t)}{\max(G(t))} \tag{4}$$

Each case is referred to using an acronym representing the type of stall it undergoes. Case LE is a leading-edge stall case, presented mainly to distinguish its flow characteristics from mixed/trailing-edge stall. We additionally simulated case LE using URANS to make comparisons with LES, and we present those results in Appendix B. Case MX undergoes a mixed stall. One case that could be classified as either mixed or trailing-edge stall (MXTE) and one case that clearly undergoes trailing-edge (TE) stall are also presented. The NACA 0012 airfoil is used for all cases, except for case MX, where we used the NACA 0018 airfoil. It can be observed from Table 1 that with increasing Re_c and decreasing pitch rate, the tendency is toward trailing-edge stall. Similarly, an increase in thickness tends to lead to trailing-edge stall [28]. We carried out one other case with a maximum pitch rate that was one-fifth that of the TE. At such a low pitch rate, we found that there was no DSV formation, and therefore have not included the results here.

Figure 3a compares the kinematics of all the cases. The variation in α is plotted with nondimensional time, $t^*(= tU_\infty/c)$, and scaled using the convective time scale of the flow. The nondimensional pitch rate K, which is defined as the maximum value of $(1/2)d\alpha_{\text{rad}}/dt^*$ for each case (where α_{rad} is α in radians), represents the level of unsteadiness or phase lag between the pitching and fluid motions [25]. Cases LE, MX, MXTE, and TE have moderate to high K values ($0.025 \le K \le 0.075$). The freestream flow Mach number Ma is 0.1 in the LES. For reference, we have also shown time scaled using kinematics (Fig. 3b) for the high-Re_c cases using the transformation $\hat{t} = t^*/t_{\text{scale}} - t_{\text{offset}}$, where t_{scale} is a scaling factor equal to max $(t^*)/2$ for each case and t_{offset} is chosen such that $\alpha_{\max}$ lies at $\hat{t} = 1$.

C. LESP and BEF Definitions

The LESP, which is a measure of the suction at the leading edge, can be calculated from CFD or experimental results using surface pressure data [17]. The approach is rooted in the fact that, when the stagnation point is not at the geometric leading edge of the airfoil, the flow is forced to travel around the rounded leading edge. This flow curvature gives rise to a low-pressure region near the leading edge. The net force acting on the leading edge is resolved into components acting along and normal to the direction of the camber line at the leading edge. The component of force along the camber line is a "suction" force acting in the forward direction. The leading-edge force on the airfoil, obtained by integrating the surface pressure on the forward portion of the airfoil from the leading edge to the x/c for the maximum-thickness location [denoted by $(x/c)_{\max}$], is then split into its suction and normal components. When these components are nondimensionalized by the net dynamic pressure ($q_\infty = \rho U_\infty^2/2$, where ρ is the freestream density) and chord, we obtain the coefficients of suction $C^{\text{ref}}_{s,\text{LE}}$ and normal force $C^{\text{ref}}_{n,\text{LE}}$ on the leading edge:

$$C^{\text{ref}}_{s,\text{LE}} = F_{S,\text{LE}}/q_\infty c \tag{5}$$

$$C^{\text{ref}}_{n,\text{LE}} = F_{N,\text{LE}}/q_\infty c \tag{6}$$

As shown by Ramesh et al. [37], thin-airfoil theory gives the relationship between $C^{\text{ref}}_{s,\text{LE}}$ and LESP as

$$C^{\text{ref}}_{s,\text{LE}} = 2\pi(\text{LESP})^2 \tag{7}$$

The sign of the LESP is set to be the same as that of the $C^{\text{ref}}_{n,\text{LE}}$ so that positive $C^{\text{ref}}_{n,\text{LE}}$ is assumed to correspond to a flow with stagnation point on the lower surface, and vice versa. Additionally, to ensure compatibility with theory, the CFD/experiment-derived LESP is set to zero at the few time instants when the $C^{\text{ref}}_{s,\text{LE}}$ has a negative value.

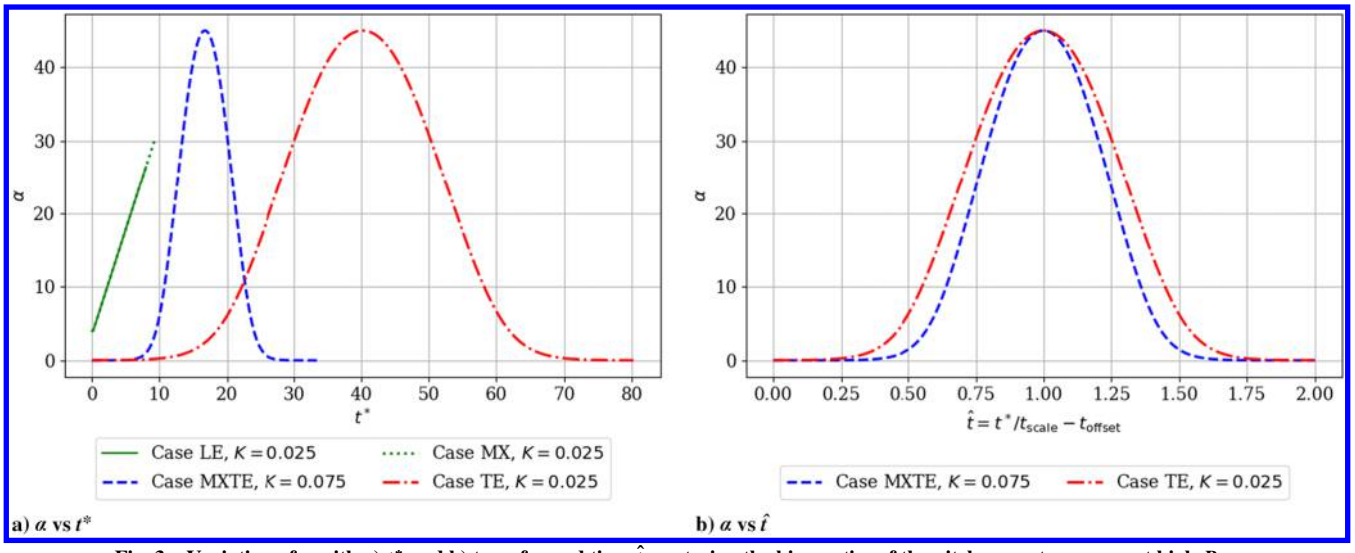

Fig. 3 Variation of α with a) t^* and b) transformed time $\hat{t}$, centering the kinematics of the pitch-up–return cases at high Re_c.

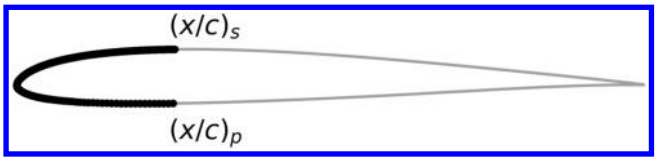

Fig. 4 Schematic showing limits of integration for calculating BEF and LESP. x/c for BEF set to 0.01 based on prior results [18]; x/c for LESP set to location of maximum airfoil thickness [17].

Thus, the LESP is calculated from $C^{\text{ref}}_{s,\text{LE}}$ and $C^{\text{ref}}_{n,\text{LE}}$ as

$$\text{LESP} = \begin{cases} \text{sgn}(C^{\text{ref}}_{n,\text{LE}})\sqrt{\frac{C^{\text{ref}}_{s,\text{LE}}}{2\pi}}, & \text{for } C^{\text{ref}}_{s,\text{LE}} > 0 \\ 0, & \text{for } C^{\text{ref}}_{s,\text{LE}} \le 0 \end{cases} \tag{8}$$

Next, we define the second parameter under consideration, namely, the boundary enstrophy flux. Enstrophy is the square of the vorticity magnitude $|\boldsymbol{\omega}|^2$. This simplifies to ω^2, which is the square of the spanwise vorticity, for 2-D flow. We consider the integral of its flux from the wall, i.e., $\partial(\omega^2/2)/\partial n = \omega(\partial\omega/\partial n)$, as defined in Eq. (9). The spanwise vorticity ω has been normalized by U_∞/c, and the normal and tangential directions to the airfoil surface (n and s, respectively) have been normalized by c. A factor of $1/Re_c$ is included so that the BEF can be viewed as a product of the vorticity ω and boundary vorticity flux defined as $(1/Re_c)\partial\omega/\partial n$. The integral is carried out between x/c on the pressure side to x/c on the suction side, as shown in Fig. 4:

$$\text{BEF} = \frac{1}{Re_c}\int_{(x/c)_p}^{(x/c)_s} \omega\frac{\partial\omega}{\partial n}\,\text{d}s \tag{9}$$

The BEF can be thought of as the integral of the product of vorticity and streamwise pressure gradient, due to the proportional growth of the vorticity flux and the streamwise pressure gradient at the wall: that is, $(1/Re_c)\partial\omega/\partial n \sim (1/\rho)\partial p/\partial s$ for small tangential surface acceleration. Therefore, large contributions to the BEF arise only from regions of high vorticity combined with large pressure gradients. Recent work on leading-edge dynamic stall onset [18] has shown that the dominant contribution arises from the laminar leading-edge region where there is large favorable pressure gradient/clockwise vorticity as flow accelerates around the leading edge. Due to this property of the BEF, it is nearly independent of integration length, as long the region very close to the leading-edge is included. Therefore, the integral for BEF is carried out over 1% chord (that is, from $0.01c$ on the pressure side to $0.01c$ on the suction side). The BEF increases in magnitude as the favorable pressure gradient at the leading edge grows. When the favorable pressure gradient drops with LSB burst, the BEF magnitude also drops after reaching a maximum. Because the bursting of the LSB occurs before DSV formation in leading-edge stall, the BEF reaches its maximum magnitude before DSV formation and effectively signals stall onset. However, in trailing-edge stall, leading-edge suction tends to persist for longer [23], even with the prevalence of large regions of reverse flow downstream. It is therefore expected that the peak magnitude of the BEF (and the LESP) would occur later. This necessitates further investigation into the applicability of these stall criteria to mixed/trailing-edge stall.

In the following section, we first present the method used to classify stall across cases. We then compare flow features across cases representing different stall types and investigate the applicability of the max(LESP) and max(|BEF|) criteria as indicators for dynamic stall onset.

IV. Results and Discussion

A. Stall Classification

Following Ref. [1], we differentiate between leading-edge, mixed, and trailing-edge stall based on the propagation of flow reversal boundaries over the suction surface. Figure 5 shows the loci of these boundaries for three URANS cases (LE, MXTE, and TE), representing leading-edge, mixed/trailing-edge, and trailing-edge stall. The solid curves represent points on the suction surface where C_f first goes to zero. The regions where C_f values have a very small magnitude (less than 1×10^{-4}) are identified by the enclosing shaded bands. For case LE, flow reversal originates near the leading edge and propagates downstream with increasing angle of attack. For the trailing-edge stall case, flow reversal originates at the trailing edge and moves upstream. The curve corresponding to case MXTE illustrates the reason for its classification in between mixed and trailing-edge stall. Based on the solid curve, it could be classified as undergoing trailing-edge stall. However, if the upper boundary were considered, it could be considered mixed stall because flow reversal around $x = 0.15c$ seems to move downstream and merge with the flow reversal propagating upstream from the trailing edge. The faster rate of reverse flow propagation at the trailing edge for the higher pitch-rate case (MXTE) is also seen from Fig. 5.

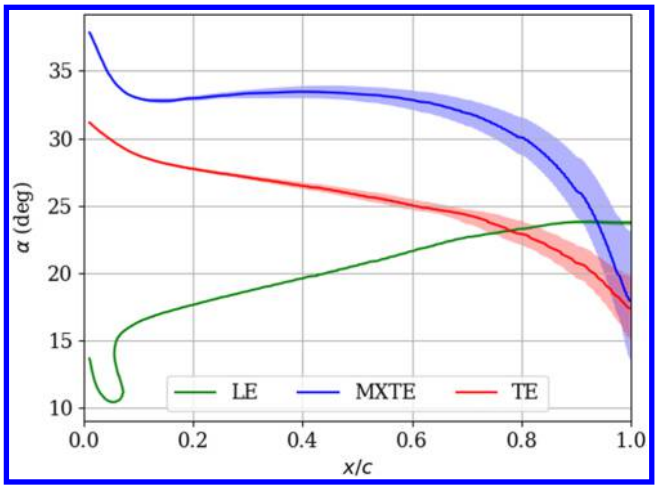

Fig. 5 Flow reversal boundaries for different stall (URANS) cases.

B. Comparison Between Leading-Edge and Mixed Stall from LES Results

Space–time contours of the friction coefficient C_f on the suction surface of the airfoil are used to elucidate the sequence of flow events that occur as the unsteady motion progresses. Figure 6a shows the space–time diagram on the suction surface for the NACA 0012 airfoil undergoing a constant-rate pitch-up motion at $Re_c = 2\times10^5$. This corresponds to case LE in Table 1. The x axis represents the chordwise distance on the suction surface and the y axis represents the angle of attack, with relevant flow events marked in the figure. As the airfoil pitches up, the transition point moves upstream, with the eventual formation of an LSB due to laminar separation and turbulent reattachment of the boundary layer [38]. As α increases, at a certain point, the LSB fails to reattach due to the insurmountable adverse pressure gradient downstream of the suction peak, and it breaks down or bursts. After the bursting of the LSB, flow characteristics are dominated by the DSV, for which the imprint on the airfoil surface (shown in blue) is seen convecting downstream. Although some flow reversal is seen at the trailing edge, it is insignificant.

On the contrary, in a mixed stall, as shown for the NACA 0018 airfoil for the same maneuver and Re_c (case MX) in Fig. 6b, the flow reversal at the trailing edge is predominant and interacts with the leading edge. We find that a large region of trailing-edge reverse flow is present before the collapse of leading-edge suction (around $\alpha = 22.7$ deg) for this case. There is boundary-layer breakdown at the leading edge from the bursting of the LSB as well as upstream propagation of trailing-edge separated flow, with their subsequent merging. When these flows interact around at around 23 deg, there is negative C_f over the entire airfoil suction surface (compare with C_f contours for case LE in Fig. 6a, where this never happens). This behavior agrees with the definition of mixed stall by McCroskey et al. [21]. The DSV is seen convecting downstream after the interaction

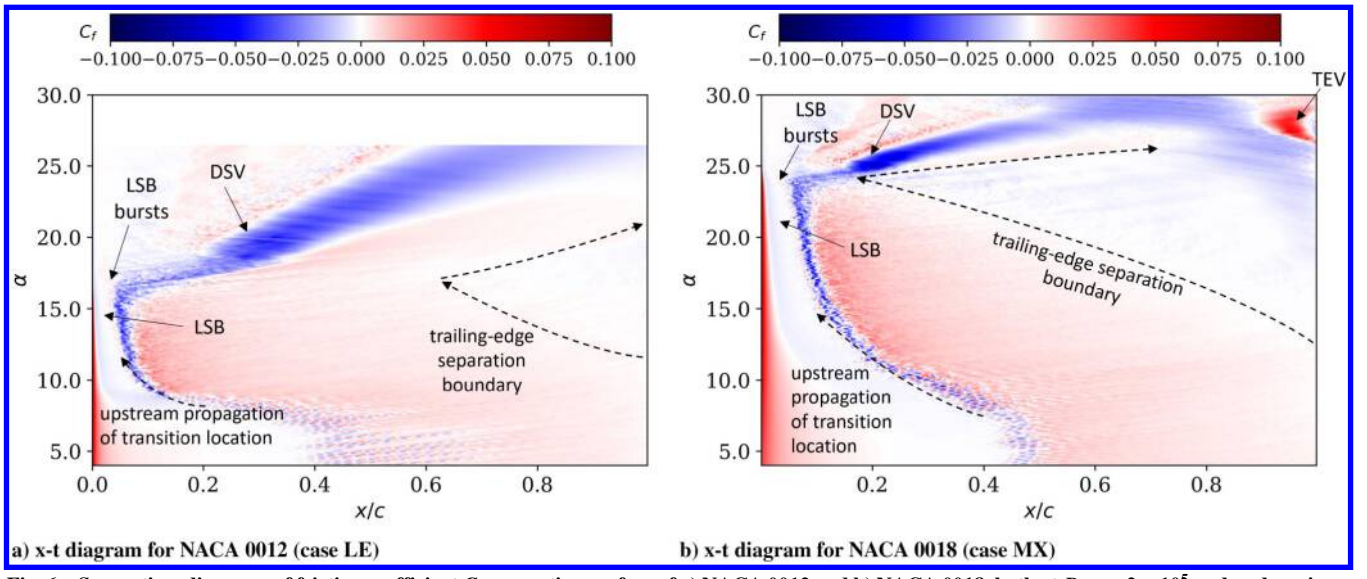

Fig. 6 Space–time diagrams of friction coefficient C_f on suction surface of a) NACA 0012 and b) NACA 0018, both at $Re_c = 2 \times 10^5$ and undergoing a constant-rate pitch-up maneuver. Flow reversal originating from trailing edge is much more significant for mixed stall (Fig. 6b) as compared to leading-edge stall (Fig. 6a).

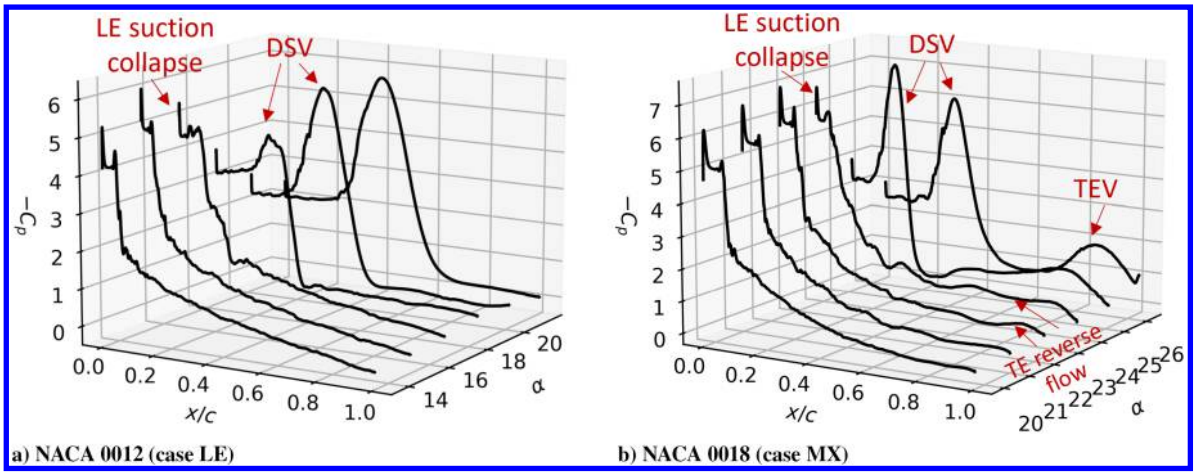

Fig. 7 C_p profiles on the suction side at a few α showing features of a) leading-edge stall and b) mixed stall.

between leading- and trailing-edge separated flows. The larger thickness of the NACA 0018 airfoil has the effect of postponing the point of stall onset along the time axis because the adverse pressure gradient following the suction peak at the leading edge is lower. Figure 7 shows C_p profiles at a few α for the two cases, contrasting the flow features between leading-edge and mixed stall. The leading-edge suction collapse is less abrupt for case MX, with the presence of significant trailing-edge reverse flow regions.

For pure trailing-edge stall, the reverse flow region propagating upstream from the trailing edge tends to dominate flow dynamics as the airfoil pitches up. In general, trailing-edge-type stall is expected for thicker airfoils and/or higher Re_c. Due to the large computational expense of LES, particularly at higher Re_c, we have used URANS simulations to study cases evincing unsteady mixed/trailing-edge stall. Appendix B compares LES and URANS results for case LE, demonstrating that the trends match closely.

Next, we examine the effect of the more significant trailing-edge separation observed for case MX relative to case LE on the stall criteria under consideration. Figures 8a and 8b show the variation in the LESP (black) and |BEF| (green) with time for cases LE and MX, respectively. The vertical dashed lines signify the location of their maxima. The instances of DSV formation (solid orange) and lift stall (dashed–dotted red) are also marked. The top panel within each figure shows the variation of α with time for reference. We will evaluate the LESP and BEF criteria against whichever point occurs earlier (DSV formation or lift stall) for each case. Clearly, both parameters exhibit critical behavior (i.e., reach their maximum magnitudes) in the vicinity of stall onset. For case LE, both parameters reach their maxima in advance (between 0.1 and 0.4 Δt^* ahead, where $\Delta t^* = \Delta t U_\infty / c$) of DSV formation. The BEF reaches its maximum magnitude about $0.3\Delta t^*$ earlier as compared to the LESP, mimicking the trend of the favorable pressure gradient at the leading edge. Lift stall follows well after DSV formation in the leading-edge stall case due to the strong DSV that remains over the airfoil surface, contributing to vortex-induced lift. A similar trend is observed for case MX, with both parameters reaching their maximum magnitudes about $0.7\Delta t^*$ ahead of DSV formation. An interesting point to note is that the delay between DSV formation and lift stall has narrowed considerably due to the significantly larger trailing-edge separation present in case MX relative to case LE. DSV formation occurs $3\Delta t^*$ before lift stall for case LE while occurring just $0.6\Delta t^*$ before lift stall for case MX. The trailing-edge separation in case MX covers over 50% of the airfoil chord (see Fig. 6b), resulting in a loss of circulation and lift stall, despite the vortex-induced lift contributed by the DSV. For both cases, LE and MX, the LESP and BEF parameters signal stall onset in advance of DSV formation.

C. URANS Results for Higher-Re_c Cases

The higher-Re_c cases (MXTE and TE) carried out using URANS are discussed in this section to further investigate the effect of

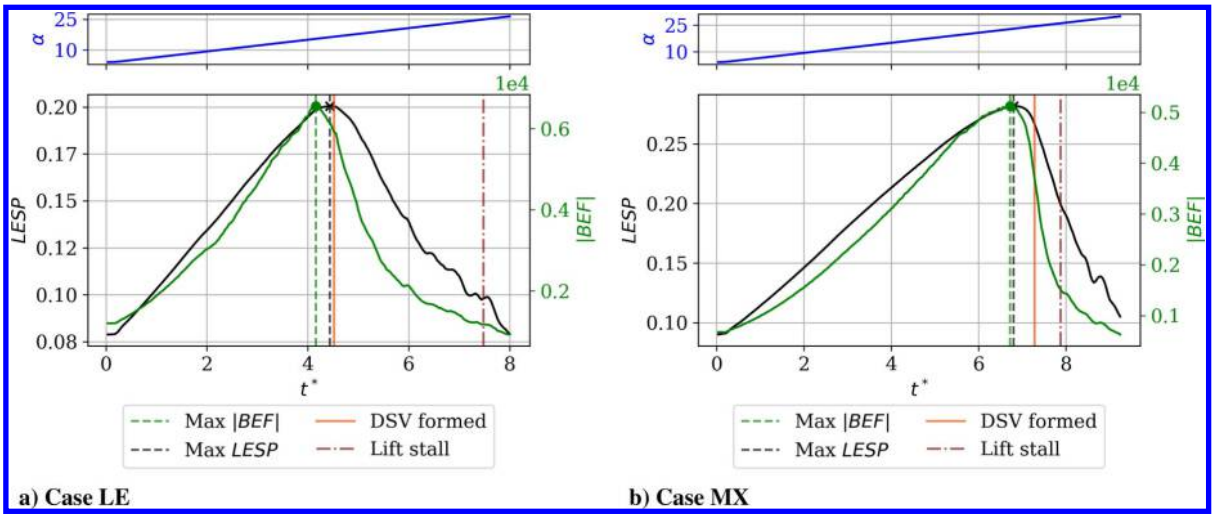

Fig. 8 Variations of LESP (black) and BEF (green) for a) leading-edge stall and b) mixed stall.

unsteady trailing-edge separation on the stall-onset predictive capability of the max(LESP) and max(|BEF|) criteria.

1. Case MXTE: NACA 0012, $Re_c = 3 \times 10^6$, and $K = 0.075$

Case MXTE corresponds to the NACA 0012 airfoil undergoing a pitch-up–return motion at a nondimensional pitch rate of 0.075, pivoted about the quarter-chord point.

Figures 9a–9c show the variation of the coefficient of lift C_l, drag C_d, and moment C_m about the quarter-chord point, respectively, with t^*. Figure 9d shows the variation in the maximum magnitude of C_p near the leading-edge (up to 5% chord on the suction surface) with t^*. The variation of α with time is coplotted with C_l in Fig. 9a for reference. Note that Figs. 9a–9c show the unsteady aerodynamic coefficients that are integrated quantities, whereas Fig. 9d shows the variation of max($|C_p|$) near the leading edge, which is a point quantity. We observe three instances between t^* of 13 and 20 where C_m diverges: the first of which is located at $t^* = 13.6$ and signifies moment stall. The gradual variation of C_m can initially be attributed to the gradual growth in the extent of the trailing-edge reverse flow. The moment stall point is approximately marked to represent the noticeable negative divergence of C_m. Moment stall is also accompanied by a large increase in C_d as the reverse flow region grows. Leading-edge suction collapses next, at around $t^* = 14.3$. Lift stall then follows, at around $t^* = 14.7$.

The space–time contours of $-C_p$ and C_f shown in Figs. 10a and 10b point out some of the features observed during the unsteady motion of the airfoil. A sequence of vorticity contours overlaid with streamlines is presented in Fig. 11. As the airfoil pitches up, reverse flow from the trailing edge moves upstream, as shown in Fig. 10b. The expanding region of reverse flow leads to the divergence in C_m observed in Fig. 9c. The reverse flow interacts with the leading-edge flow, resulting in the formation of a strong DSV around $0.2c$, which is pointed out in the C_p space–time contours. Because it is hard to determine if the trailing-edge reverse flow has reached all the way up to the leading edge before DSV formation, we have classified this case as being in between the mixed and trailing-edge stall. The imprint of the DSV (in yellow in Fig. 10a) can be seen moving downstream in the C_p contours. The downstream convection of the DSV further contributes to negative C_m. The DSV also contributes to increased lift (note increased lift slope in Fig. 9a) over the airfoil surface. A lift stall results when the DSV convects away from the airfoil surface. The flowfield at the lift stall point is shown in Fig. 11b. Because α continues to increase beyond the lift stall point, there is vortex shedding from the trailing edge (Fig. 11c). Although the

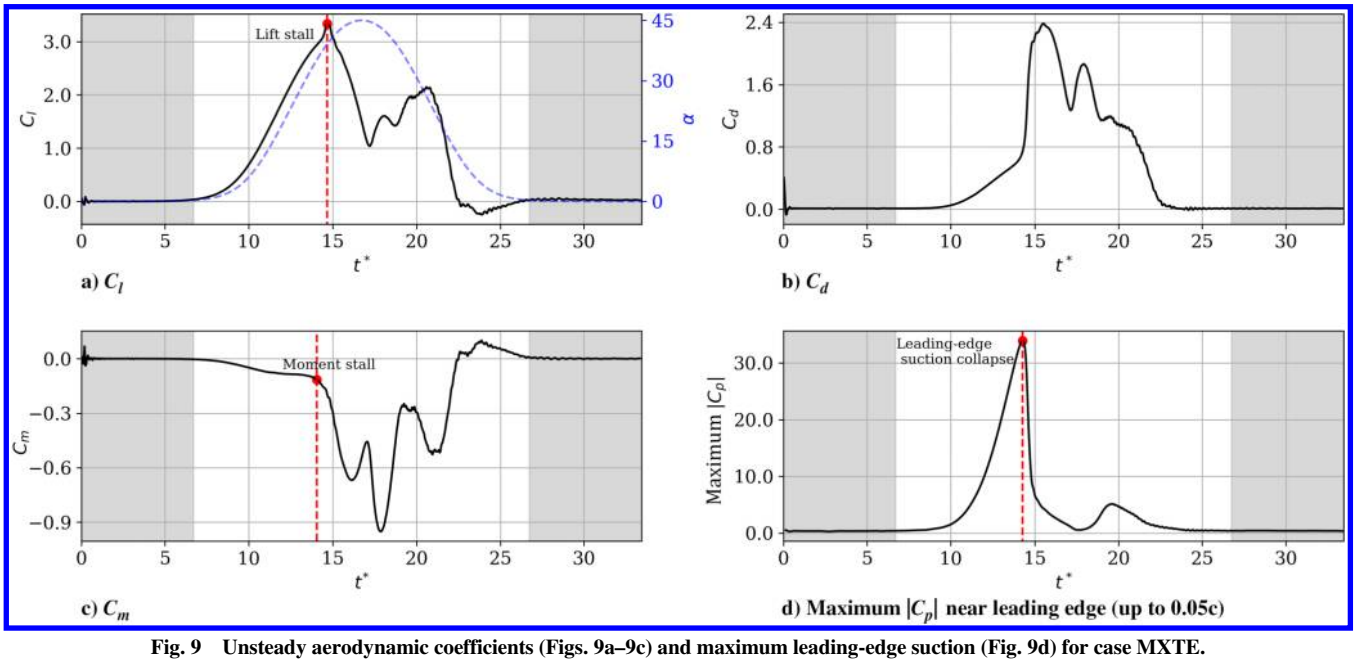

Fig. 9 Unsteady aerodynamic coefficients (Figs. 9a–9c) and maximum leading-edge suction (Fig. 9d) for case MXTE.

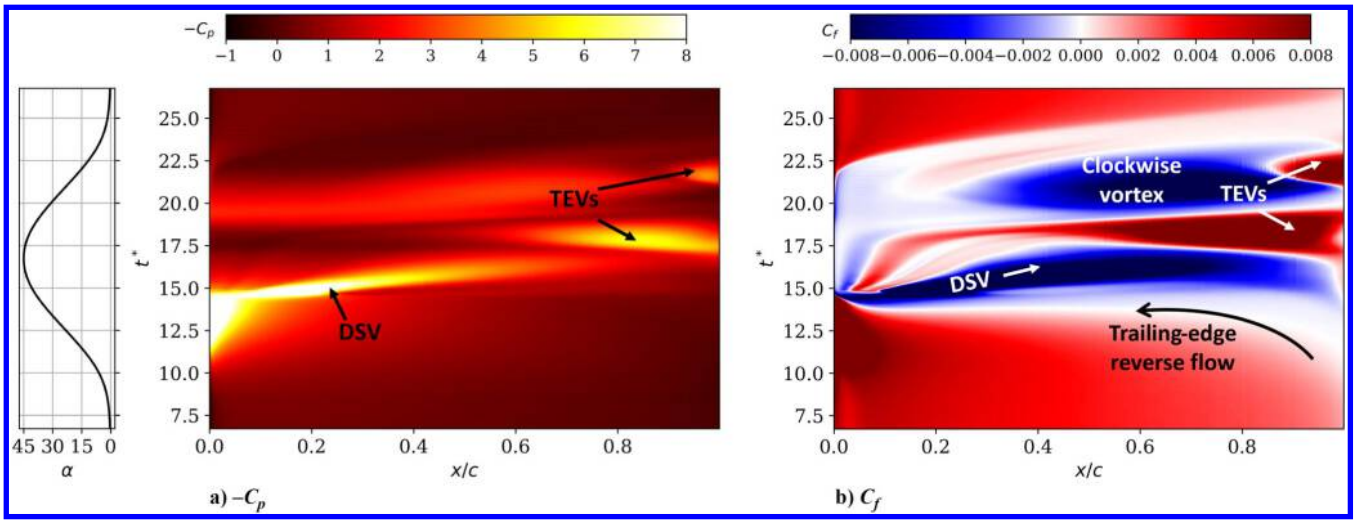

Fig. 10 Space–time contours of a) $-C_p$ and b) C_f for case MXTE.

trailing-edge vortex (TEV) contributes only to a small increase in lift, it induces a large pitch-down moment due to the longer moment arm (trailing edge to quarter-chord point). This explains the second deviation in C_m in Fig. 9c. By this point, the angle of attack has begun to decrease, and the TEV is shed. A clockwise vortex develops (as shown in Fig. 10b) as the TEV sheds, contributing to a further increase in lift. The formation and downstream propagation of this vortex explain the third deviation in C_m. Around $t^* = 20.6$ (Fig. 11e), with decreasing α, this vortex detaches from the leading edge and moves away from the airfoil surface.

Figure 12 shows the variation of the LESP and BEF for case MXTE. Despite the larger extent of flow separation, we observe that the parameters reach their maximum magnitudes about $0.3\Delta t^*$ before DSV formation. Lift stall follows closely ($0.2\Delta t^*$) after DSV formation. Therefore, the two criteria effectively signal stall onset for case MXTE. For the higher-Re_c cases with pitch-up–return motion [the current case (MXTE) as well as case TE, discussed in Sec. IV.C.2], where leading-edge suction recovers to some extent as α decreases during the pitch-down part of the motion, the LESP reaches a second peak. Because the LESP represents a camberwise force (same as the chordwise force for symmetric airfoils), leading-edge suction recovery rotates the force vector toward the leading edge, resulting in an increase in the chordwise component. The BEF does not show significant secondary peaks for any of the cases. This simply reflects the much lower magnitude of C_p of the secondary peaks relative to the first. The ratio of the C_p magnitude of the second peak relative to the first for case MXTE (identified from Fig. 9d) is about 0.14. The leading-edge suction magnitude as the flow reestablishes during pitch-down is much weaker. This is doubly reflected in the favorable pressure gradient and the clockwise vorticity at the leading edge, which is captured by the BEF. Therefore, there is a larger disparity in BEF magnitudes between the first and second peaks as compared to the LESP.

2. *Case TE: NACA 0012, $Re_c = 3 \times 10^6$, and $K = 0.025$*

Case TE has similar kinematics to case MXTE, except at a lower pitch rate. Figures 13a–13c show the variation in unsteady aerodynamic coefficients with t^*, and Fig. 13d shows the variation in $\max(|C_p|)$ near the leading edge. Moment stall, leading-edge suction collapse, and lift stall occur in quick succession in that order, around $t^* = 30$. As will be explained shortly, the subsequent oscillations in the aerodynamic coefficients are due to vortex shedding. Figures 14a and 14b show the space–time contours of $-C_p$ and C_f. As seen from the C_f contours, boundary-layer flow reversal begins at the trailing edge at about $t^* = 25$. Due to the lower pitch rate, the upstream propagation of flow reversal is much more gradual. As the reverse flow region grows in extent, moment stall occurs at $t^* = 28$. Leading-edge suction collapses shortly afterward at $t^* = 29.9$. A DSV develops around the quarter-chord point, and its downstream propagation is marked in the C_p contours. Lift stall follows at $t^* = 30.7$, when the DSV is shed. As α continues to increase beyond lift stall, the airfoil acts like a bluff body, leading to vortex shedding alternately from the leading and trailing edges at a nondimensional frequency ($f^+ = fc/U_\infty$) of about 0.2. This is clearly seen from the contour plots in Fig. 14 and is reflected in the oscillations in the aerodynamic coefficients in Fig. 13. The TEVs subsequently cause several large deviations in C_m due to the longer moment arm. The duration of vortex shedding and the strength of the shed vortices are higher compared to case MXTE. This is explained as follows. Lift stall occurs at a lower α for case TE compared to case MXTE on account of the pitch rate for case MXTE being three times as high. Therefore, $\alpha_{\max}$ is reached sooner after lift stall and flow recovery commences earlier for case MXTE. In contrast, there is about 15 deg of pitch-up motion remaining when lift stall occurs for case TE, thereby delaying flow recovery induced by the decreasing the angle of attack. The vortex shedding continues until shortly after $\alpha_{\max}$ is attained and the angle of attack reduces. Once flow begins to reattach with reduction in α, there is circulation recovery over the airfoil surface. The lift recovers and then reduces as α goes to zero.

Figure 15 shows vorticity contours overlaid with streamlines for different points in the motion. Figures 15a–15c show the flowfield around the times of moment stall, leading-edge suction drop, and lift stall. Figures 15d and 15e show the vortex shedding that occurs after lift stall is reached, and Fig. 15f shows the reestablished attached flow at low-α during pitch-down.

The variations of the LESP and BEF with t^* for the current case are shown in Fig. 16. The observed trend remains similar to the other cases with significant trailing-edge separation. Both parameters reach their maximum magnitudes approximately $0.7\Delta t^*$ before DSV formation. Lift stall follows closely ($0.2\Delta t^*$) after DSV formation. Thus, we conclude that both criteria are effective stall-onset indicators for the current trailing-edge stall case.

In summary, we find that the max(LESP) and max(|BEF|) criteria signal leading-edge, mixed, and trailing-edge stall in advance of DSV formation, based on cases LE, MX, MXTE, and TE. We attribute this to leading-edge suction collapsing before DSV formation for all the cases under consideration (this will be corroborated further in Sec. IV.D). We also note a smaller delay between DSV formation and lift stall as trailing-edge separation becomes more significant.

D. Comparing Leading-Edge, Mixed, and Trailing-Edge Stall

Figure 17 provides a timeline showing the stall criteria relative to the occurrence of relevant events such as trailing-edge separation, moment stall, leading-edge suction collapse [$\max(|C_p|)$], DSV formation, and lift stall. The top two panels are for the LES ramp cases at the lower Re_c, whereas the bottom two panels are for the URANS pitch-up–return cases at the higher Re_c. Although we make some

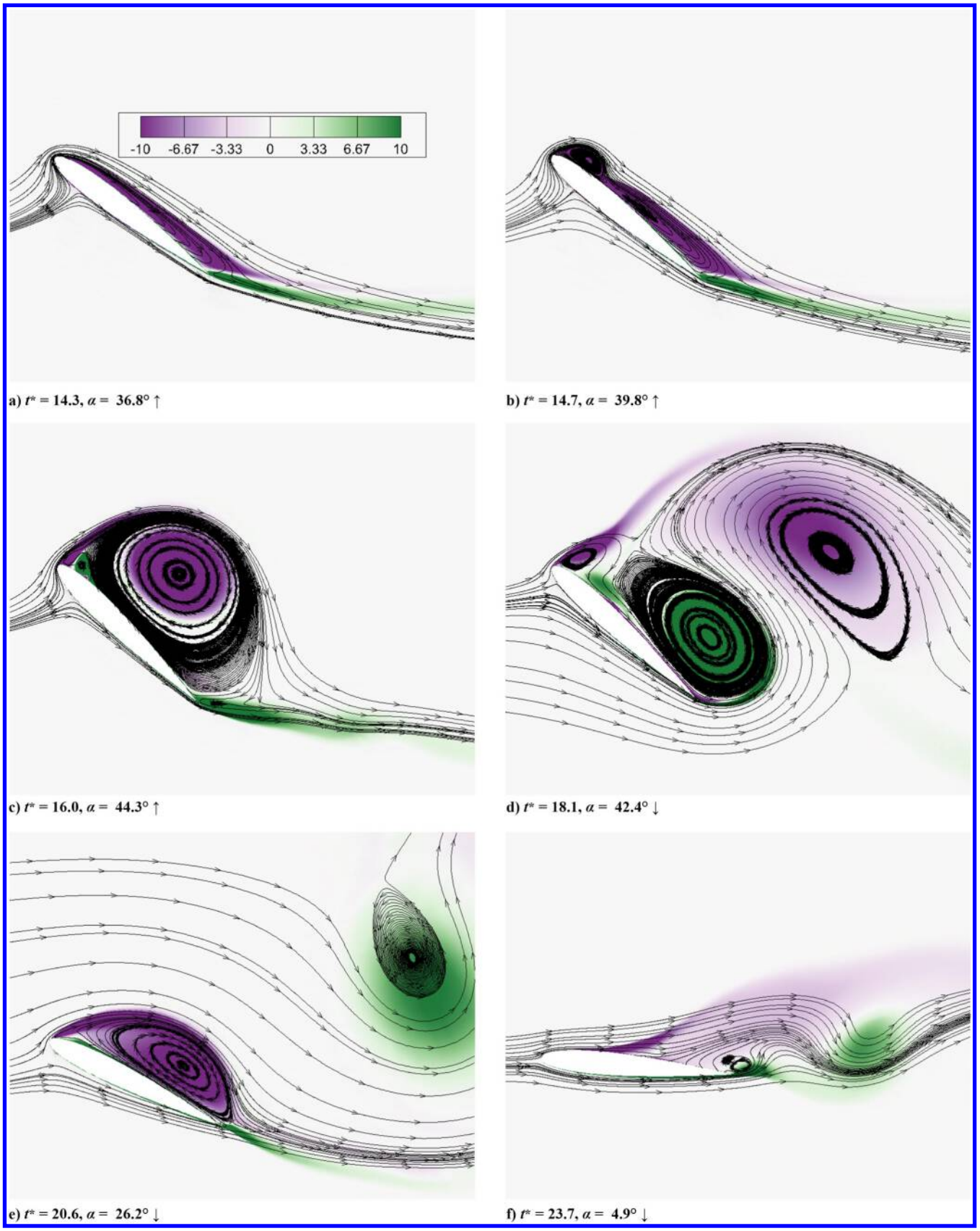

Fig. 11 Vorticity contours overlaid with streamlines for case MXTE (directions of arrows in subcaptions refer to pitch-up (↑) or pitch-down (↓) part of motion; contour legend shown in Fig. 11a). Events shown are a) leading-edge suction drop, b) lift stall, c–d) subsequent vortex shedding, e) clockwise vortex leading to lift recovery, and f) attached flow at low α.

general comments on the trends, direct comparisons are possible only within each group, with the caveat that they include very few data points. The line marking the stall-onset criteria is at their average location because they are close, especially for the cases with larger trailing-edge separation. The point marking trailing-edge separation is plotted at the α when reverse flow from the trailing-edge reaches $0.95c$. Max($|C_p|$) marks the instance of maximum magnitude of the pressure coefficient near the leading edge.

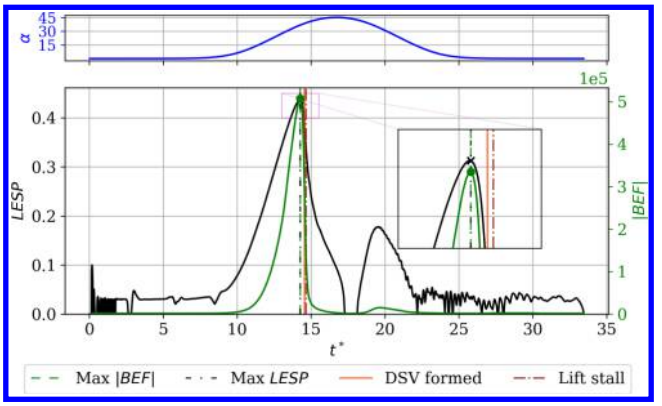

Fig. 12 Variations of LESP (black) and BEF (green) for MXTE that undergoes mixed/trailing-edge stall.

We note that the sequence of events goes as follows:

$$\text{trailing-edge separation} \rightarrow \text{moment stall} \rightarrow \max(|C_p|) \rightarrow \text{DSV formation} \rightarrow \text{lift stall}$$

for cases MX, MXTE, and TE. For case LE, the preceding sequence varies, in that moment stall occurs after DSV formation. Therefore, moment stall is clearly due to the downstream propagation of a coherent DSV in case LE, whereas the expanding region of trailing-edge reverse flow causes C_m to diverge early in the other cases and is not solely attributed to the DSV. For all cases, the leading-edge stall criteria [max(LESP) and max(|BEF|)], shown with black lines, occur very close to the instance of suction collapse [max($|C_p|$)] at the leading edge (purple diamond symbols). Another general trend is the narrowing gap between leading-edge suction collapse and lift stall as trailing-edge separation becomes more significant.

The ramp cases at lower Re_c (top two panels of Fig. 17) vary only in the airfoil used. Trailing-edge separation occurs earlier for case MX, which consists of a thicker NACA 0018 airfoil, in comparison to case LE, which consists of an NACA 0012 airfoil. All other events are postponed for the thicker airfoil, which experiences, at a given α, a lower adverse pressure gradient at the leading edge due to the larger radius of curvature. However, they occur closer together compared to case LE.

The pitch-up–return cases at higher Re_c (bottom two panels of Fig. 17) vary only in their pitch rates. Case MXTE has a higher pitch rate as compared to case TE. Trailing-edge separation and all the

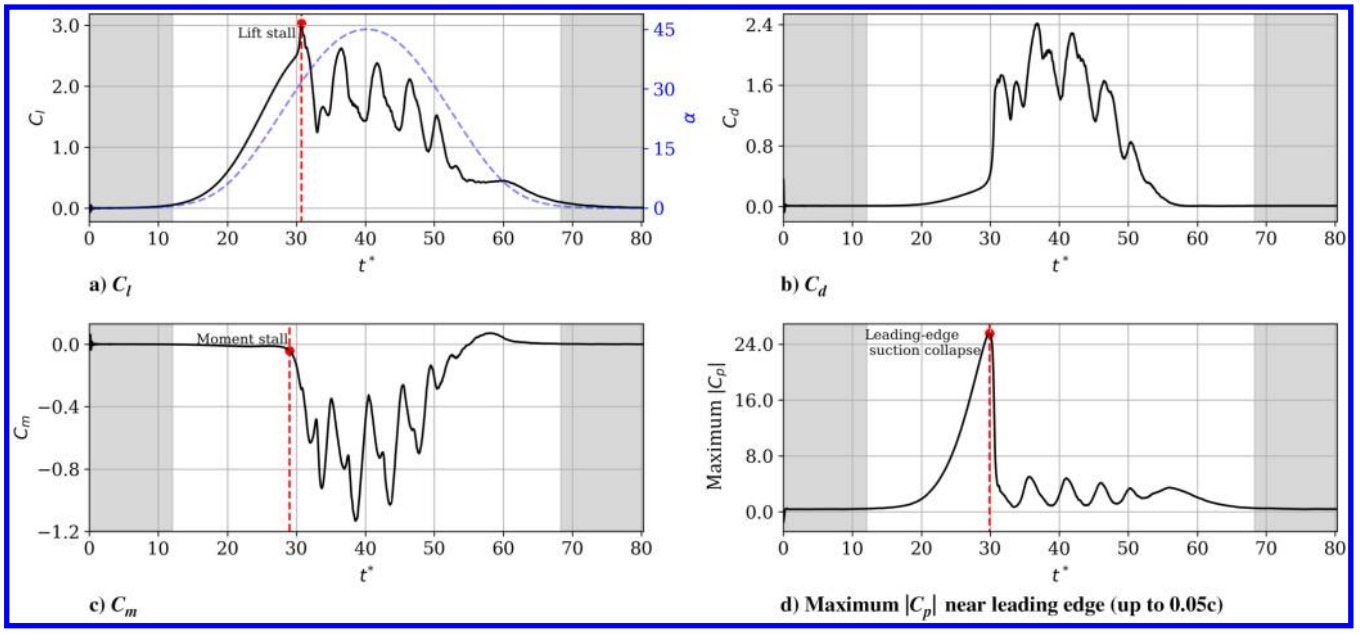

Fig. 13 Case TE: a–c) unsteady aerodynamic coefficients, and d) maximum leading-edge suction.

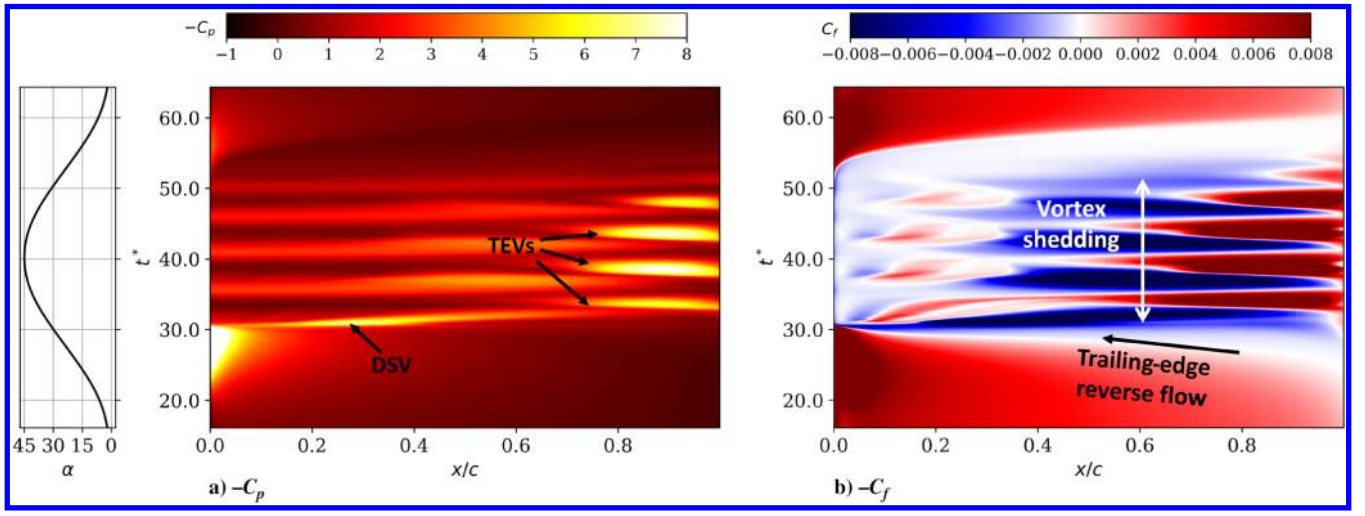

Fig. 14 Space–time contours of a) $-C_p$ and b) C_f for case TE.

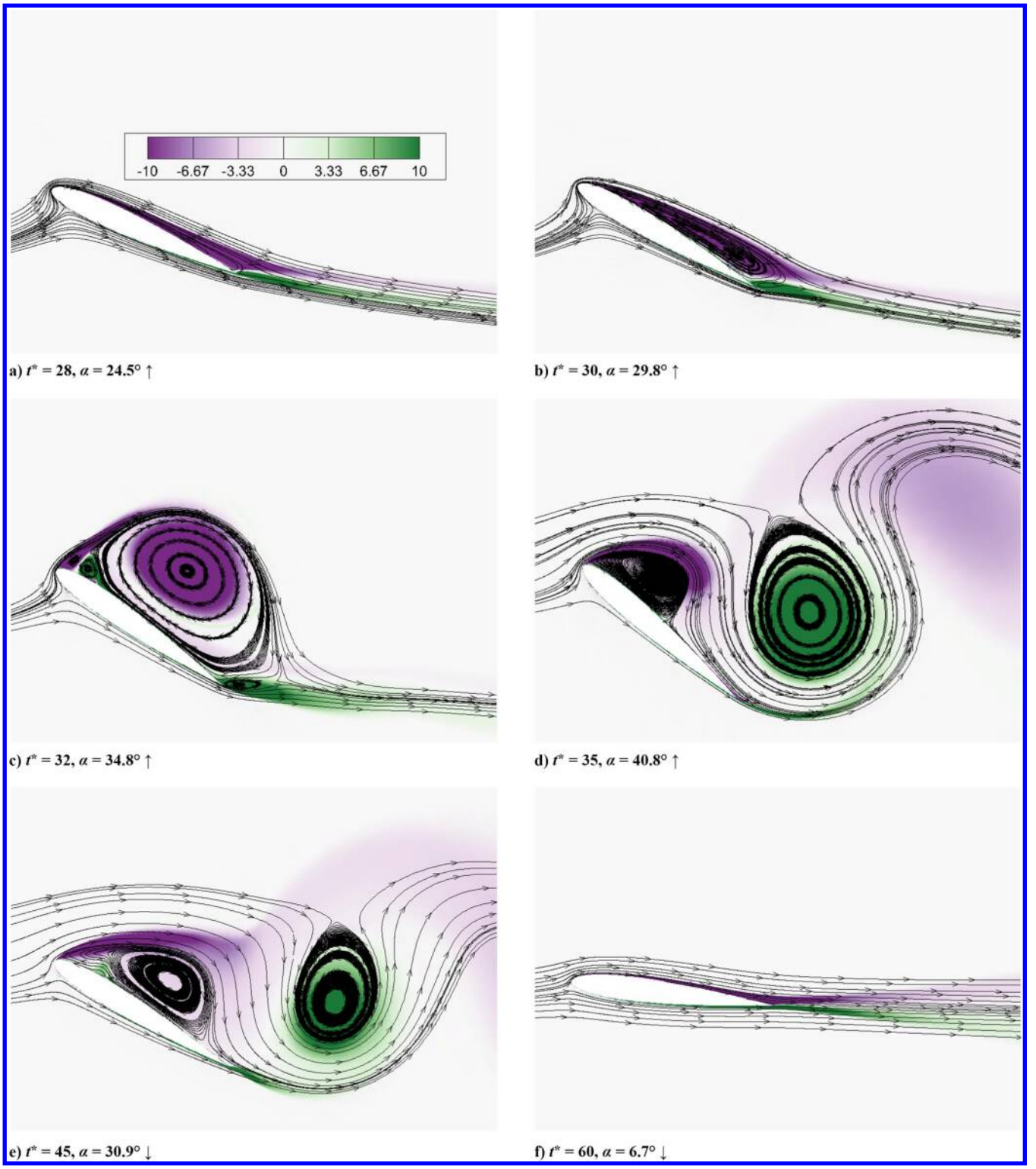

Fig. 15 Vorticity contours overlaid with streamlines for case TE (directions of arrows same as in Fig. 11; contour legend shown in Fig. 15a): a–c) flowfield around moment stall, leading-edge suction drop, and lift stall; d–e) vortex shedding after lift stall; and f) reestablishment of attached flow at low α after pitch-down.

subsequent events occur at a lower α for case TE due to smaller time-lag effects. The gap between max($|C_p|$) and DSV formation is smaller for case TE. We note again that these observations are to be taken with caution because they involve limited data points. Lift stall occurs closer to the maximum α of 45 deg for case MXTE relative to case TE, resulting in a smaller duration of vortex shedding. A stronger DSV is formed for the larger pitch rate case MXTE, which is consistent with observations from the literature [39]. Additional cases may need to be analyzed to make remarks on more general trends across different stall types.

Finally, the stall-onset criteria nearly coincide with the leading-edge suction collapse or instance of max($|C_p|$) near the leading edge for all cases. For all four cases involving a DSV in the stall process, the criteria are reached before DSV formation. This is attributed to leading-edge suction collapse occurring before DSV formation for all these cases. Based on the cases analyzed, we find the max(LESP) and

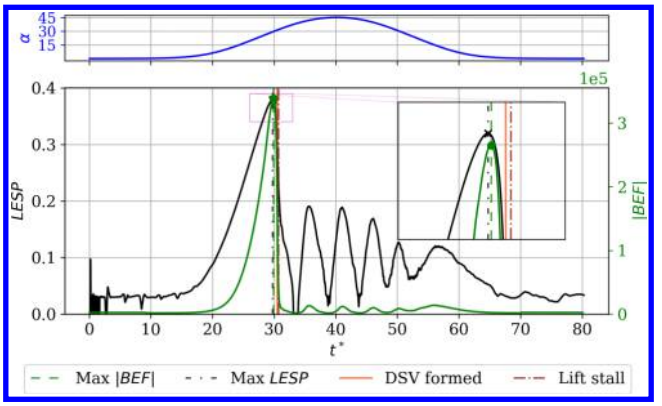

Fig. 16 Variations of LESP (black) and BEF (green) for Case TE that undergoes trailing-edge stall.

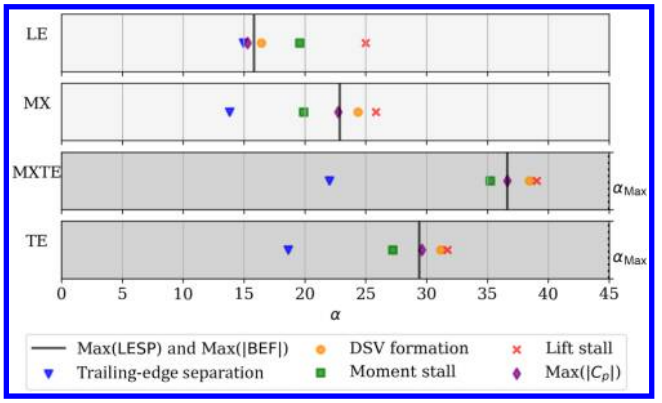

Fig. 17 Timeline (in terms of α) of important events for all cases. Top two panels show LES ramp cases at lower Re_c, whereas bottom two panels show URANS pitch-up–return cases at higher Re_c.

max(|BEF|) criteria to be effective indicators of stall onset where the DSV plays a prominent role.

V. Conclusions

The objective of the present study was to evaluate two leading-edge-based stall-onset criteria, namely, max(LESP) and max(|BEF|), for mixed and trailing-edge stall. The LESP is the camberwise force near the leading edge, which is a pressure-based parameter. The BEF is a vorticity-based parameter that represents the product of vorticity and streamwise pressure gradient near the leading edge. Both parameters have been previously demonstrated to effectively signal onset in leading-edge stall for $Re_c \sim \mathcal{O}(10^5)$, where there was an abrupt collapse in leading-edge suction. In the present work, the max(LESP) and max(|BEF|) criteria were evaluated for mixed and trailing-edge stall, where there was significant trailing-edge separation. The key point of interest was to verify if the criteria were reached in advance of critical points such as DSV formation and lift stall under these conditions. Mixed/trailing-edge stall was generally expected to occur at higher Re_c and/or for thicker airfoils. Four cases of airfoils undergoing unsteady pitching motion were considered, with varying extents of trailing-edge separation, with DSV formation playing an important role in the stall process. These cases were simulated at a moderate Re_c of 2×10^5 using wall-resolved LES, and at a high Re_c of 3×10^6 using unsteady RANS. Using the definitions and characteristics of leading-edge, mixed, and trailing-edge stalls from the literature, the features of the different cases were contrasted in detail. The LESP and BEF parameters were evaluated for each case representing a specific stall type, and it was observed that they reached their maximum magnitudes in advance of DSV formation for all of them. Lift stall followed DSV formation, with smaller delay as the study moved toward more trailing-edge-dominated stall. Based on the cases analyzed, it is concluded that the leading-edge stall criteria, max(LESP) and max(BEF), are effective even for cases with significant trailing-edge separation where the DSV plays a prominent role.

Appendix A: Mesh-Sensitivity Studies

A.1. LES

A mesh-sensitivity study is carried out for static as well as dynamic simulations for flow over a NACA 0012 airfoil at $Re_c = 2 \times 10^5$. Four mesh sizes are evaluated. Static simulations are performed with the airfoil at angle of attack of $\alpha = 4$ deg. For the dynamic simulations, a constant-rate pitch-up motion about the airfoil quarter-chord point is considered. Three mesh sizes are evaluated. The overall grid dimensions and first cell size in wall units ($\Delta x^+, \Delta y^+, \Delta z^+$) for the static simulation are presented in Table A1. The values of x^+, y^+, and z^+ are well below the values recommended in the literature for LES.

Figure A1 plots the results of the mesh refinement study for static-airfoil simulations using LES. Spatial distributions of the aerodynamic pressure coefficient C_p and skin-friction coefficient C_f, are compared. All four grids capture the transition location (at $x/c \approx 0.45$) on the suction surface. The coarse grid shows a slightly shorter laminar separation bubble, as seen by inspecting the C_f plot (Fig. A1b). Furthermore, the medium, fine, and finest grids show an extended transition region as compared to the coarse grid. The difference between the medium, fine, and finest grids is small.

Figure A2 plots the time histories of the sectional lift and drag coefficients, c_l and c_d, respectively. The differences between the coarse grid and the other three grids are more apparent in the dynamic simulation results. But, the medium, fine, and finest grids exhibit very similar time histories. Based on this study, the fine grid was selected for the simulations.

A.2. URANS

A mesh-sensitivity study for the URANS model was conducted using the NACA 0012 airfoil. The baseline grid, which is used in the present work, has a y^+ of 1.0 at $Re_c = 3 \times 10^6$. Two additional grids were generated with y^+ of 5.0 and 0.5. The wall-normal grid spacings in wall units y^+ are listed in Table A2 for the three grids used in this study: at $Re_c = 30{,}000$ and 3×10^6.

The three grids were used to study the aerodynamic behavior, especially the LESP, of the NACA 0012 airfoil for two extreme ends of the parameter space: 2) pitch rate and $K = 0.05$ with pivot at the leading edge, and 2) $K = 0.60$ with pivot at the trailing edge. This study was conducted for both values of Reynolds number Re ($= 30{,}000$ and 3×10^6). Figure A3 shows the max(LESP) values [corresponding to leading-edge vortex (LEV) initiation] for the NACA 0012 airfoil for these three grids at the two Re_c. It is seen that the change in max(LESP) between the three grids is small and is close to the error in the LESP. This error, indicated by the error bar in Fig. A3, is the typical difference in the LESP between the successive time instants at which CFD output is used to calculate the LESP.

Table A1 Grid dimensions and nondimensional cell sizes in wall units ($\Delta x^+, \Delta y^+, \Delta z^+$)[a]

Grid	$N_\xi \times N_\eta \times N_\zeta$[b]	Δy^+ (average maximum)	Δx^+ (average maximum)	Δz^+ (average maximum)
Coarse	$395 \times 643 \times 51$	0.36, 0.94	22.0, 55.1	17.0, 63.9
Medium	$410 \times 995 \times 101$	0.18, 0.47	14.3,85.2	8.5, 32.4
Fine	$410 \times 1341 \times 134$	0.19, 0.50	10.6,87.2	7.0, 24.5
Finest	$615 \times 1490 \times 150$	0.12, 0.32	9.6, 56.7	5.7,2 1.7

[a]Averages and maximum values of cell sizes are over the entire airfoil; the suction side of the airfoil is more refined than the pressure side.

[b]N_ξ, N_η, and N_ζ refer to the number of points in the radial, circumferential, and span directions, respectively.

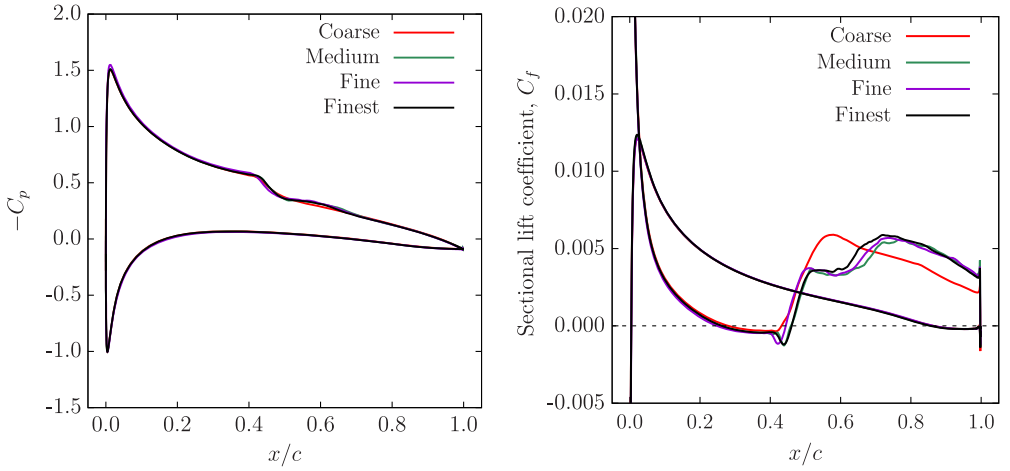

a) Pressure coefficient, C_p b) Skin-friction coefficient, C_f

Fig. A1 LES mesh-sensitivity study results for static simulations of flow over NACA 0012 airfoil at $\alpha = 4$ deg and $Re_c = 2 \times 10^5$. Distributions of a) C_p and b) C_f over the airfoil surface.

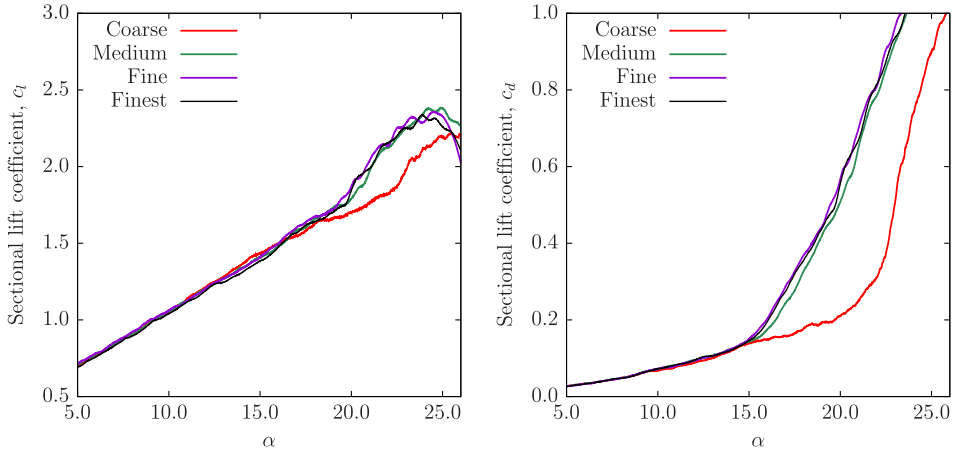

a) Variation of c_l with α b) Variation of c_d with α

Fig. A2 LES mesh-sensitivity study results for dynamic simulations for a constant-rate pitch-up maneuver. Time histories of a) c_l and b) c_d are plotted as functions of angle of attack α.

Table A2 y^+ values for the grids used for URANS mesh-sensitivity study

Grid	y spacing at wall, m	y^+ at $Re = 30{,}000$	y^+ at $Re_c = 3 \times 10^6$
1	5.17×10^{-5}	0.069	5.0
2 (baseline)	1.03×10^{-5}	0.014	1.0
3	5.17×10^{-6}	0.0069	0.5

Appendix B: Comparison of LES and URANS Results for Case LE

Figure B1 compares the unsteady aerodynamic coefficients between LES (black solid) and URANS (pink dashed) for case LE. We see that the peak values of the coefficients occur slightly later for URANS. For example, lift stall (peak in C_l) is shifted by about 0.4 deg aft. Also, finer variations in the coefficients due to small-scale structures that are generated are not captured in URANS, as

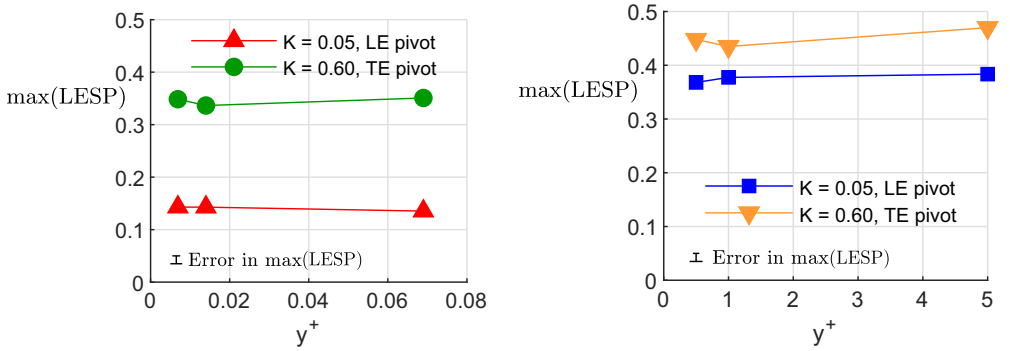

a) $Re_c = 30{,}000$ b) $Re_c = 3 \times 10^6$

Fig. A3 Max(LESP) variation with grid y^+ at LEV initiation for a) $Re_c = 30{,}000$ and b) $Re = 3 \times 10^6$.

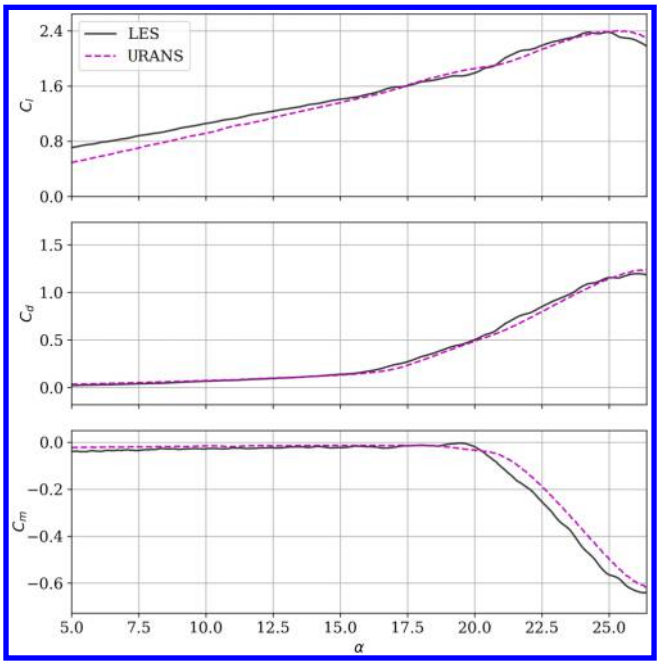

Fig. B1 Comparison of unsteady aerodynamic coefficients between LES and URANS for case LE.

expected. However, the overall match in terms of magnitudes and trends of the aerodynamic coefficients is quite good.

Figure B2 compares the variation of the LESP and |BEF| between LES and URANS. For both parameters, URANS overpredicts the maximum value and shifts it aft in time; so, we present their variation normalized by the maximum value of each. For the LESP, this shift is about 0.7 deg; whereas for BEF, it is closer to 1 deg. The maximum value is overpredicted by 4% for the LESP and 10% for BEF. These larger discrepancies for the BEF could be because its calculation involves higher-order derivatives at the wall as opposed to the LESP, which uses C_p. Small errors in mean quantities such as C_p are amplified with higher-order derivatives. Also, higher-order wall-normal gradients are captured far more accurately by LES. However, our primary interest is in capturing the trend of the variation, which is achieved by URANS. Therefore, for our purposes [i.e., identifying the max(LESP) and max(|BEF|) criteria relative to DSV formation], we only consider their peak locations in time. The slight shifts in the peaks of the quantities between LES and URANS are acceptable because there is a corresponding aft shift in time for all other events, such as DSV formation and lift stall. We therefore use URANS for evaluating the aforementioned criteria for higher-Re_c cases.

Figure B3 compares the space–time contours of C_f between LES and URANS. The contours corresponding to LES capture small-scale features, whereas the URANS results are smoothed out because such features are not captured. However, features such as DSV propagation and trailing-edge separation and reattachment are

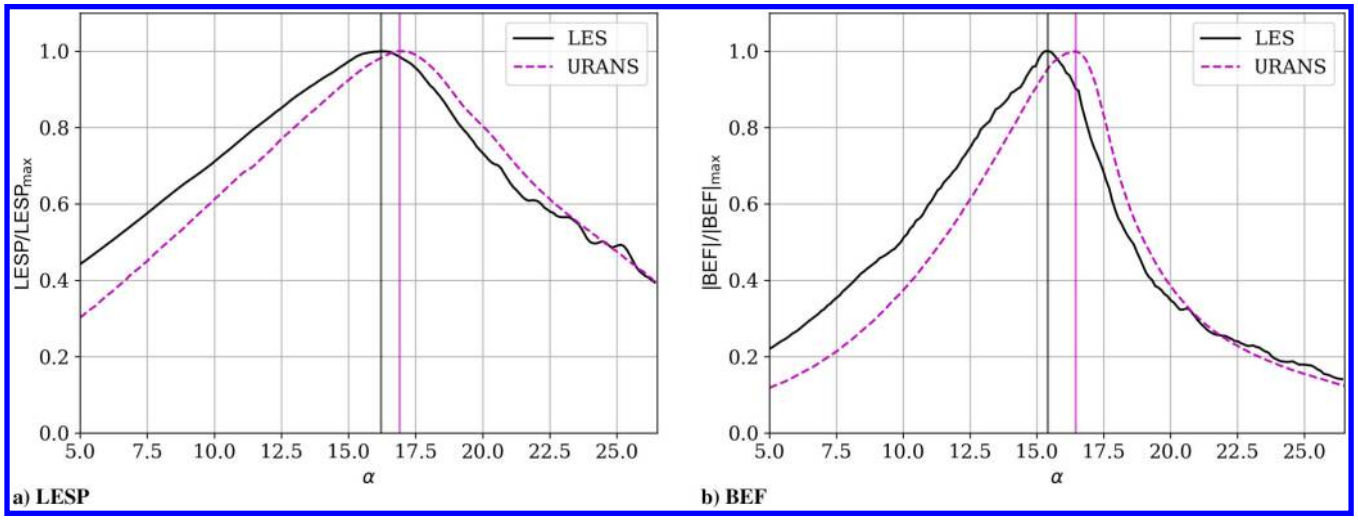

Fig. B2 Comparison of a) LESP and b) |BEF| from LES and URANS normalized by their maximum values for case LE.

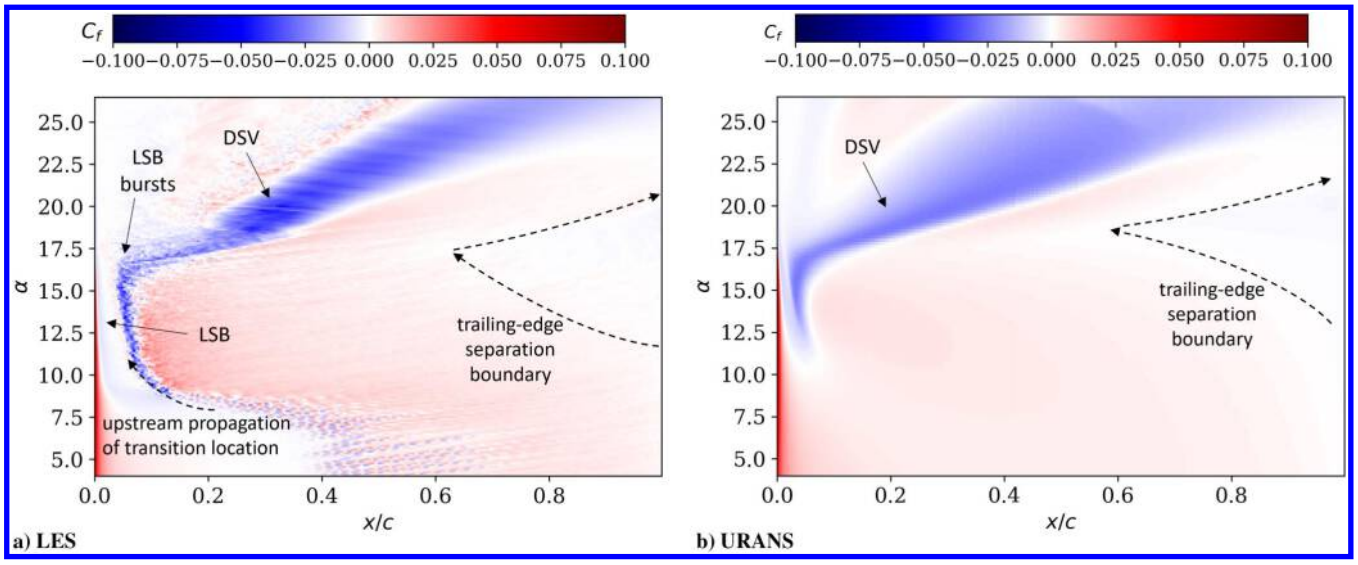

Fig. B3 C_f space–time contours from a) LES and b) URANS for case LE.

broadly captured well, although there is a slight shift aft in α for the URANS cases. We find this to be acceptable for the purpose of relative comparisons of the stall-onset criteria with the critical points such as DSV formation and lift stall.

Acknowledgments

Funding for this research was provided by the National Science Foundation (NSF; grants CBET-1554196 and 1935255). A. Sharma acknowledges the support provided to him by the 2019 and 2021 U.S. Air Force Office of Scientific Research Summer Faculty Fellowships. Computational resources were provided by the NSF Extreme Science and Engineering Discovery Environment (XSEDE) (grant no. TG-CTS130004) and the Argonne Leadership Computing Facility, which is a U.S. Department of Energy Office of Science User Facility supported under contract DE-AC02-06CH11357. S. Narsipur acknowledges Jack Edwards of North Carolina State University for the REACTMB-INS code used for the computations in this effort. The authors acknowledge the assistance by Miguel Visbal and Daniel Garmann from the U.S. Air Force Research Laboratory in providing initial large-eddy simulation solutions.

References

[1] McCroskey, W. J., "The Phenomenon of Dynamic Stall," NASA TM 81264, Washington, D.C., 1981.

[2] Müller-Vahl, H. F., Nayeri, C. N., Paschereit, C. O., and Greenblatt, D., "Dynamic Stall Control via Adaptive Blowing," *Renewable Energy*, Vol. 97, Nov. 2016, pp. 47–64, https://www.sciencedirect.com/science/article/pii/S0960148116304633. https://doi.org/10.1016/j.renene.2016.05.053

[3] Santra, S., and Greenblatt, D., "Dynamic Stall Control Model for Pitching Airfoils with Slot Blowing," *AIAA Journal*, Vol. 59, No. 1, 2021, pp. 400–404. https://doi.org/10.2514/1.J059818

[4] Lombardi, A. J., Bowles, P. O., and Corke, T. C., "Closed-Loop Dynamic Stall Control Using a Plasma Actuator," *AIAA Journal*, Vol. 51, No. 5, 2013, pp. 1130–1141. https://doi.org/10.2514/1.J051988

[5] Yu, H., and Zheng, J., "Numerical Investigation of Control of Dynamic Stall over a NACA0015 Airfoil Using Dielectric Barrier Discharge Plasma Actuators," *Physics of Fluids*, Vol. 32, No. 3, 2020, Paper 035103. https://doi.org/10.1063/1.5142465

[6] Rice, T. T., Taylor, K., and Amitay, M., "Pulse Modulation of Synthetic Jet Actuators for Control of Separation," *Physical Review Fluids*, Vol. 6, No. 9, 2021, Paper 093902. https://doi.org/10.1103/PhysRevFluids.6.093902

[7] Chandrasekhara, M. S., "Compressible Dynamic Stall Vorticity Flux Control Using a Dynamic Camber Airfoil," *Sadhana*, Vol. 32, No. 1, 2007, pp. 93–102. https://doi.org/10.1007/s12046-007-0008-8

[8] Leishman, J. G., and Beddoes, T. S., "A Semi-Empirical Model for Dynamic Stall," *Journal of the American Helicopter Society*, Vol. 34, No. 3, 1989, pp. 3–17.

[9] Sheng, W., Galbraith, R. A. M., and Coton, F. N., "A New Stall-Onset Criterion for Low Speed Dynamic-Stall," *Journal of Solar Energy Engineering*, Vol. 128, No. 4, 2005, pp. 461–471. https://doi.org/10.1115/1.2346703

[10] Ramesh, K., Gopalarathnam, A., Granlund, K., Ol, M. V., and Edwards, J. R., "Discrete-Vortex Method with Novel Shedding Criterion for Unsteady Aerofoil Flows with Intermittent Leading-Edge Vortex Shedding," *Journal of Fluid Mechanics*, Vol. 751, July 2014, pp. 500–538. https://doi.org/10.1017/jfm.2014.297

[11] Narsipur, S., Gopalarathnam, A., and Edwards, J. R., "Low-Order Modeling of Airfoils with Massively Separated Flow and Leading-Edge Vortex Shedding," *AIAA Aerospace Sciences Meeting*, AIAA Paper 2018-0813, Jan. 2018.

[12] Deparday, J., and Mulleners, K., "Critical Evolution of Leading Edge Suction During Dynamic Stall," *Journal of Physics: Conference Series*, Vol. 1037, No. 2, 2018, Paper 022017. https://doi.org/10.1088/1742-6596/1037/2/022017

[13] Deparday, J., and Mulleners, K., "Modeling the Interplay Between the Shear Layer and Leading Edge Suction During Dynamic Stall," *Physics of Fluids*, Vol. 31, No. 10, 2019, Paper 107104. https://doi.org/10.1063/1.5121312

[14] Kay, N. J., Richards, P. J., and Sharma, R. N., "Low-Reynolds Number Behavior of the Leading-Edge Suction Parameter at Low Pitch Rates," *AIAA Journal*, Vol. 60, No. 3, 2021, pp. 1721–1729. https://doi.org/10.2514/1.J060733

[15] Saini, A., Narsipur, S., and Gopalarathnam, A., "Leading-Edge Flow Sensing for Detection of Vortex Shedding from Airfoils in Unsteady Flows," *Physics of Fluids*, Vol. 33, No. 8, 2021, Paper 087105.

[16] Li, X., and Feng, L.-H., "Critical Indicators of Dynamic Stall Vortex," *Journal of Fluid Mechanics*, Vol. 937, April 2022, Paper A16. https://doi.org/10.1017/jfm.2022.30.

[17] Narsipur, S., Hosangadi, P., Gopalarathnam, A., and Edwards, J. R., "Variation of Leading-Edge Suction During Stall for Unsteady Aerofoil Motions," *Journal of Fluid Mechanics*, Vol. 900, Oct. 2020, Paper A25. https://doi.org/10.1017/jfm.2020.467.

[18] Sudharsan, S., Ganapathysubramanian, B., and Sharma, A., "A Vorticity-Based Criterion to Characterise Leading Edge Dynamic Stall Onset," *Journal of Fluid Mechanics*, Vol. 935, March 2022, Paper A10. https://doi.org/10.1017/jfm.2021.1149

[19] Gault, D. E., "A Correlation of Low-Speed, Airfoil-Section Stalling Characteristics with Reynolds Number and Airfoil Geometry," NACA TN 3963, 1957.

[20] Carr, L., McAlister, K., McCroskey, W., Aeronautics, U. S. N., and Administration, S., "Analysis of the Development of Dynamic Stall Based on Oscillating Airfoil Experiments," NASA TN D-8382, 1977.

[21] McCroskey, W. J., McAlister, K. W., Carr, L. W., Pucci, S. L., Lambert, O., and Indergrand, R. F., "Dynamic Stall on Advanced Airfoil Sections," *Journal of the American Helicopter Society*, Vol. 26, No. 3, 1981, pp. 40–50.

[22] Sudharsan, S., Narsipur, S., and Sharma, A., "Evaluating Dynamic Stall Onset Criteria for Mixed and Trailing-Edge Stall," AIAA Paper 2022-1983, 2022. https://doi.org/10.2514/6.2022-1983

[23] McCullough, G. B., and Gault, D. E., "Examples of Three Representative Types of Airfoil-Section Stall at Low Speed," NACA TN 2502, 1951.

[24] Eldredge, J., Wang, C., and Ol, M., "A Computational Study of a Canonical Pitch-Up, Pitch-Down Wing Maneuver," AIAA Paper 2009-3687, 2009. https://doi.org/10.2514/6.2009-3687

[25] Corke, T. C., and Thomas, F. O., "Dynamic Stall in Pitching Airfoils: Aerodynamic Damping and Compressibility Effects," *Annual Review of Fluid Mechanics*, Vol. 47, No. 1, 2015, pp. 479–505. https://doi.org/10.1146/annurev-fluid-010814-013632

[26] Kiefer, J., Brunner, C. E., Hansen, M. O., and Hultmark, M., "Dynamic Stall at High Reynolds Numbers Induced by Ramp-Type Pitching Motions," *Journal of Fluid Mechanics*, Vol. 938, May 2022, Paper A10. https://doi.org/10.1017/jfm.2022.70

[27] Benton, S. I., and Visbal, M. R., "The Onset of Dynamic Stall at a High, Transitional Reynolds Number," *Journal of Fluid Mechanics*, Vol. 861, Feb. 2019, pp. 860–885. https://doi.org/10.1017/jfm.2018.939

[28] Sharma, A., and Visbal, M., "Numerical Investigation of the Effect of Airfoil Thickness on Onset of Dynamic Stall," *Journal of Fluid Mechanics*, Vol. 870, July 2019, pp. 870–900. https://doi.org/10.1017/jfm.2019.235

[29] Visbal, M. R., and Gaitonde, D. V., "On the Use of Higher-Order Finite-Difference Schemes on Curvilinear and Deforming Meshes," *Journal of Computational Physics*, Vol. 181, No. 1, 2002, pp. 155–185.

[30] Li, Y., and Wang, Z., "A Priori and a Posteriori Evaluations of Sub-Grid Scale Models for the Burgers' Equation," *Computers and Fluids*, Vol. 139, Nov. 2016, pp. 92–104.

[31] Garmann, D. J., Visbal, M. R., and Orkwis, P. D., "Comparative Study of implicit and Subgrid-Scale Model Large-Eddy Simulation Techniques for Low-Reynolds Number Airfoil Applications," *International Journal for Numerical Methods in Fluids*, Vol. 71, No. 12, 2013, pp. 1546–1565.

[32] Cassidy, D. A., Edwards, J. R., and Tian, M., "An Investigation of Interface-Sharpening Schemes for Multiphase Mixture Flows," *Journal of Computational Physics*, Vol. 228, No. 16, 2009, pp. 5628–5649.

[33] Spalart, P. R., and Allmaras, S. R., "A One-Equation Turbulence Model for Aerodynamic Flows," AIAA Paper 1992-0439, 1992.

[34] Edwards, J. R., and Chandra, S., "Comparison of Eddy Viscosity—Transport Turbulence Models for Three-Dimensional, Shock-Separated Flowfields," *AIAA Journal*, Vol. 34, No. 4, 1996, pp. 756–763.

[35] Narsipur, S., Gopalarathnam, A., and Edwards, J. R., "Low-Order Model for Prediction of Trailing-Edge Separation in Unsteady Flow," *AIAA Journal*, Vol. 57, No. 1, 2019, pp. 191–207.

[36] Granlund, K., Ol, M. V., and Bernal, L., "Experiments on Pitching Plates: Force and Flowfield Measurements at Low Reynolds Numbers," AIAA Paper 2011-0872, 2011.

[37] Ramesh, K., Gopalarathnam, A., Edwards, J. R., Ol, M. V., and Granlund, K., "An Unsteady Airfoil Theory Applied to Pitching Motions Validated Against Experiment and Computation," *Theoretical and Computational Fluid Dynamics*, Vol. 27, Nov. 2013, pp. 843–864. https://doi.org/10.1007/s00162-012-0292-8

[38] O'Meara, M. M., and Mueller, T. J., "Laminar Separation Bubble Characteristics on an Airfoil at Low Reynolds Numbers," *AIAA Journal*, Vol. 25, No. 8, 1987, pp. 1033–1041. https://doi.org/10.2514/3.9739

[39] Acharya, M., and Metwally, M. H., "Unsteady Pressure Field and Vorticity Production over a Pitching Airfoil," *AIAA Journal*, Vol. 30, No. 2, 1992, pp. 403–411. https://doi.org/10.2514/3.10931

I. Gursul
Associate Editor